Geophysical Journal International

Geophys. J. Int. (2010) **180,** 375–404 doi: 10.1111/j.1365-246X.2009.04417.x

The ShakeOut earthquake scenario: Verification of three simulation sets

Jacobo Bielak,[1] Robert W. Graves,[2] Kim B. Olsen,[3] Ricardo Taborda,[1] Leonardo Ramírez-Guzmán,[1,*] Steven M. Day,[3] Geoffrey P. Ely,[4] Daniel Roten,[3] Thomas H. Jordan,[4,5] Philip J. Maechling,[5] John Urbanic,[6] Yifeng Cui[7] and Gideon Juve[4]

[1] *Computational Seismology Laboratory, Department of Civil and Environmental Engineering, Carnegie Mellon University, Pittsburgh,* PA 15213-3890, *USA. E-mail: rtaborda@andrew.cmu.edu*
[2] *URS Corporation, 566 El Dorado Street, Pasadena,* CA 91101, *USA*
[3] *Department of Geological Sciences, San Diego State University, San Diego,* CA 92182, *USA*
[4] *Department of Earth Sciences, University of Southern California, Los Angeles,* CA 90089, *USA*
[5] *Southern California Earthquake Center,* 3651 *Trousdale Parkway, Suite 169, Los Angeles,* CA 90089, *USA*
[6] *Pittsburgh Supercomputing Center,* 300 *S. Craig Street, Pittsburgh,* PA 15213, *USA*
[7] *San Diego Supercomputing Center,* 9500 *Gilman Drive, La Jolla,* CA 92093, *USA*

Accepted 2009 October 12. Received 2009 October 7; in original form 2009 March 17

SUMMARY

This paper presents a verification of three simulations of the ShakeOut scenario, an M_w 7.8 earthquake on a portion of the San Andreas fault in southern California, conducted by three different groups at the Southern California Earthquake Center using the SCEC Community Velocity Model for this region. We conducted two simulations using the finite difference method, and one by the finite element method, and performed qualitative and quantitative comparisons between the corresponding results. The results are in good agreement with each other; only small differences occur both in amplitude and phase between the various synthetics at ten observation points located near and away from the fault—as far as 150 km away from the fault. Using an available goodness-of-fit criterion all the comparisons scored above 8, with most above 9.2. This score would be regarded as excellent if the measurements were between recorded and synthetic seismograms. We also report results of comparisons based on time–frequency misfit criteria. Results from these two criteria can be used for calibrating the two methods for comparing seismograms. In those cases in which noticeable discrepancies occurred between the seismograms generated by the three groups, we found that they were the product of inherent characteristics of the various numerical methods used and their implementations. In particular, we found that the major source of discrepancy lies in the difference between mesh and grid representations of the same material model. Overall, however, even the largest differences in the synthetic seismograms are small. Thus, given the complexity of the simulations used in this verification, it appears that the three schemes are consistent, reliable and sufficiently accurate and robust for use in future large-scale simulations.

Key words: Time series analysis; Numerical solutions; Numerical approximations and analysis; Earthquake ground motions; Seismic attenuation; Computational seismology.

1 INTRODUCTION

The finite element (FE) and finite difference (FD) methods were introduced in seismology in the late 1960s, starting for simple structures (e.g. Alterman & Karal 1968; Boore 1970, 1972; Lysmer & Drake 1972; Kelly *et al.* 1976; Archuleta & Frazier 1978; Archuleta & Day 1980). Since then we have witnessed the rise of numerical solutions, also propelled by the accelerated growth of supercomputers, especially in the last 15 yr. Among the earliest 3-D simulations done on a geographical scale large enough for synthesizing recorded earthquake data was that of Frankel & Vidale (1992), who aimed at reproducing the effects of a far-field point source from an aftershock of the 1989 Loma Prieta earthquake in the Santa Clara Valley, California, using a FDs approach. After Frankel & Vidale,

*Now at: The U.S. Geological Survey, National Earthquake Information Center, Golden, CO 80401, USA.

FDs became the standard method for large-scale earthquake simulations (e.g. Olsen *et al.* 1995a,b; Olsen & Archuleta 1996; Graves 1996a, 1998; Pitarka *et al.* 1998; Furumura & Koketsu 2000; Frankel & Stephenson 2000). Others began to implement the solution of the elastodynamic equations for fairly realistic 3-D non-planar layered systems using low-order FEs (e.g. Bao *et al.* 1996, 1998; Bielak *et al.* 1999, 2005), or high-order FE methods with diagonal mass matrix, or spectral element methods (e.g. Seriani & Priolo 1994; Faccioli *et al.* 1997; Seriani 1998; Komatitsch & Vilotte 1998; Komatitsch *et al.* 2004; Käser & Dumbser 2006; Käser & Gallovic 2008). Moderate-size problems with relatively simple geometry and geological conditions have been addressed using boundary element, coupled boundary-domain element, and discrete wavenumber methods (e.g. Bouchon & Aki 1980; Mossessian & Dravinski 1987; Kawase & Aki 1990; Bielak *et al.* 1991; Hisada *et al.* 1993; Sánchez-Sesma & Luzón 1995; Bouchon & Barker 1996; Hisada & Bielak 2003). A detailed introduction and tutorial, and a more comprehensive review of the FD, FE and hybrid FD–FE methods, with particular application to the modelling of seismic wave propagation and earthquake motion, including a thorough discussion and original contributions on the treatment of free-boundary conditions, material grid parametrization, and rheological models to consider intrinsic attenuation, can be found in a recent review paper by Moczo *et al.* (2007).

For the last 10 yr, a group of researchers working on large-scale simulations has collaborated in creating a modelling community within SCEC. One of the primary objectives of such collaboration has been to ensure, through a continuing scientific exchange of data and results, that independent modelling schemes and implementations are in agreement with each other and satisfy an acceptable level of accuracy for the simulation of complex seismic phenomena. At an early stage, the Pacific Earthquake Engineering Research Center (PEER) in collaboration with SCEC sponsored five of these modelling groups to test their simulation codes and compare results for basic wave propagation problems (Day *et al.* 2001, 2003). Qualitative comparisons from this effort were in satisfactory agreement. Later, five different codes were used to run 60 earthquake scenarios in 10 different faults in the Los Angeles region, including sites in the Los Angeles, San Fernando and San Gabriel basins, as well as rock sites in the intervening areas to characterize the source-averaged effect of basin depth on spectral acceleration in the region (Day *et al.* 2005, 2006, 2008). A quantitative comparison of some of the results of these simulations was presented by Kristekova *et al.* (2006).

Much progress has been made recently by each group, and SCEC has continued to be the coalescing force for the collaboration between these research groups. This, and the fact that according to the Working Group on California Earthquake Probabilities (2008), there is a 97 per cent probability of an earthquake of magnitude $M \geq 6.7$ in southern California in a 30-yr period, with a 59 per cent probability of such an event occurring in the southern part of the San Andreas fault, and a 37 per cent probability of a regional event being $M \geq 7.5$, has led this community to model and study large scenario earthquakes of greater complexity. The first outcome of that endeavour was the TeraShake earthquake scenario (Olsen *et al.* 2006, 2008). This study has reaffirmed the importance of source characteristics, basin, directivity, and wave guiding effects that are only visible through large-scale 3-D simulations. However, larger-scale scenarios bring along greater challenges. It thus becomes critical to ensure that the simulation results of these highly complex models be credible and practically relevant, especially since the ultimate goal of this kind of simulation is to serve as a basis for performing physics-based seismic hazard analysis.

The success of earthquake ground motion simulations can be measured through the validation and verification of the synthetic results. Validation refers to the level of agreement between synthetics and actual data. Verification, on the other hand, refers to the correctness of the implementation of a simulation scheme. Even though there have been a number of attempts at validation, the agreement between synthetics and data remains far from satisfactory, except for very low frequencies ($f < 0.1$ Hz). This is because one cannot isolate the validity of the simulation from that of other factors, such as the material model, including possible non-linearities, and the source description. One common way to reduce the influence of these factors is to use small earthquakes, whose rupture can be modelled as a point source, and limit the simulation to long periods and high shear wave velocities. Unfortunately, in most cases, the source description comes from an inversion obtained using similar, if not the same conditions as those for the forward problem. In that case one cannot determine whether the discrepancies come from the model, the source, the implementation, or all of the above. Agreement does not guarantee the validity of results because of the existing redundancy between inversion and forward simulation. An intermediate step towards validation is to perform a verification exercise of synthetic results. A successful verification helps give confidence that any discrepancies with the data are likely to be due to the material and source models, and not to algorithmic or computational errors. Verification requires 'only' that the results of the simulations agree with the expected outcome of a given mathematical model. However, difficulties arise when the expected outcome (exact solution) is unknown due to complexity of the model. Such is the case for the simulation of earthquake ground motion in large basins. An alternative approach, then, is to determine how well different sets of synthetic seismograms compare among themselves for simulations of exactly the same problem.

This paper is the result of a continuing team effort and, to our knowledge, an original attempt at verification between different simulation models for a large-scale scenario earthquake. It presents a verification of three sets of results from separate simulations of the ShakeOut earthquake scenario, version 1.1 (Jones *et al.* 2008), for $V_{s_{\min}} = 500\ \mathrm{m\,s^{-1}}$ and $f_{\max} = 0.5$ Hz. Two of the simulation models implement the finite difference method (FDM), and the third one uses the finite element method (FEM). All simulations were done on parallel computers. Comparisons are done qualitatively and quantitatively, from a regional perspective for the whole simulation domain and at a localized level for selected observation points, both in the time and in the frequency domains. We review the concept of verification in the context of computational seismology as adopted from other disciplines and discuss the importance of simulation and model verification and comparison in contrast to the concept of validation. The scenario earthquake, material model, computational methods and implementations are reviewed and their corresponding effects on the outcome are discussed. Detailed comparisons of the results of the three simulation sets are presented along with a discussion of their similarities and discrepancies.

2 THE MEANING OF VERIFICATION

The importance of verification in numerical modelling resides in the fact that unless credibility is firmly established, the intended recipients of simulation results will be tempted to see the simulation process as some sort of computer gaming. This is especially true if reality is difficult to capture in a single closed system whose outcome can be precisely derived. Such is the case of earthquake

simulation. Seismic events are by definition, complex open systems. This is because earthquakes depend on a series of factors from which we still have much to learn and which are especially difficult to characterize—the description of the source and the propagating medium, or material model. Therefore, the quality of earthquake simulations relies on the modeler's knowledge of these factors, and so does its credibility.

In modelling and simulation, the issue of credibility is intrinsically associated with the problem of verification and validation—a problem that has concerned science for centuries. The concepts of veracity and validity have profound (even philosophical) implications for modelers aiming to represent and reproduce physical phenomena and systems. There are different ways to address these and other concepts like confirmation and correctness (Kleindorfer & Ganeshan 1993; Oreskes *et al.* 1994). We adopt here the terminology for modelling credibility proposed by the Society for Modelling and Simulation International (Schlesinger *et al.* 1979). We understand 'model verification' as the 'substantiation that a computerized model represents a conceptual model within specified limits of accuracy' and 'model validation' as the 'substantiation that a computerized model within its domain of applicability possesses a satisfactory range of accuracy consistent with the intended application of the model'. In other words, model verification refers to evaluating the correctness of the implementation of a computer model when compared to the theoretical concepts on which it is based, and model validation refers to how well the simulation results compare to actual data from the real system or problem entity being modelled. These concepts have been widely used in software engineering and other computational fields and have been carefully studied by several authors (e.g. Adrion *et al.* 1982; Balci 1994; Sargent 2005).

Fig. 1 shows the modelling process adapted to the problem of earthquake simulation. This representation is based on the one established by Schlesinger *et al.* (1979) and modifications proposed by Sargent (2005). The ultimate goal of any simulation process is to be able to reproduce, up to an acceptable level of accuracy, the observations from the real system (or real world)—that is, to validate both the conceptual and simulation models by reproducing

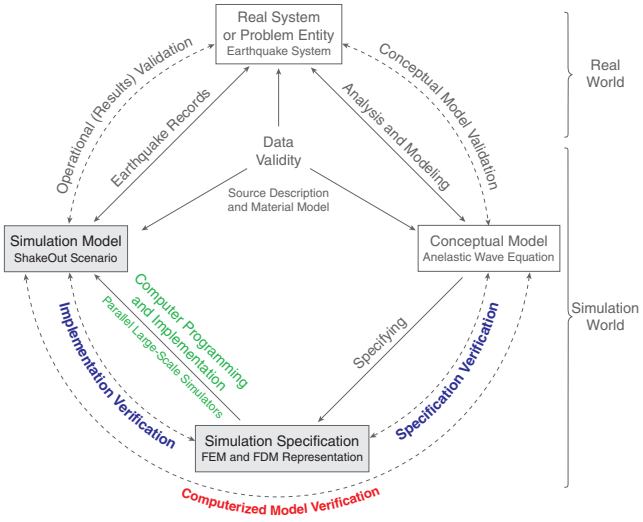

Figure 1. Simplified representation of the simulation and modelling process, and the real world and simulation world relationship with verification and validation. Modified after Schlesinger *et al.* (1979) and Sargent (2005).

experimental data or natural phenomena successfully. This corresponds to the upper half in Fig. 1. Plausible attempts to validate earthquake simulations by comparisons with real data have been done in the past (e.g. Komatitsch *et al.* 2004; Aagaard *et al.* 2008b), but we observe flaws in the process. Komatitsch *et al.* (2004), for example, fall in what Oreskes *et al.* (1994) described as *affirming the consequent*. Comparing simulation results based on a source description obtained through the same assumptions used for the forward simulation (material model, numerical approach), falls in a logical redundancy that does not necessarily validate the simulation, but does more of a verification of consistency. On the other hand, by comparing simulation sets from modelers that do not necessarily share the same core elements, as done by Aagaard *et al.* (2008b), one cannot determine the source of the discrepancies beyond affirming that they are all rational representations of the system—this is only 'face validation' or 'graphical comparison' (see Balci 1994). Even if possible, obtaining a 'perfect' match between simulation results and experimental data does not prove the model *is* real or correct. It simply 'confirms' the model. However, one must concede to the cases mentioned above that, the greater the number and diversity of confirming observations, the more probable it is that the model conceptualization and implementation is not flawed (Oreskes *et al.* 1994). In hindsight, we think that the use of the term 'validation' has been, in some cases, overstated. That is why it is so important to do 'verification' of simulations between different modelers that use the same scenarios and core assumptions.

In addition, we must consider that the earthquake scenario used in this study is hypothetical. This means that the system being modelled is non-observable and we lack a real system to compare with in terms of operational validation. We are restricted to compare our simulations with respect to the conceptual model. Such conceptual model is the mathematical abstraction of the linear momentum equation, constitutive model, and source description that are translated into a simulation specification—which in our case refers to the solution by means of FEM and FDM. Unfortunately, the complexity of the scenario being modelled does not allow one to obtain a closed solution of the conceptual model. This restricts our options even more, and we are left with the option of performing a 'computerized model verification' by means of comparison with other models that share the same basic assumptions and input data. This corresponds to the lower half of the circle representing the simulation process (Fig. 1), which is precisely the scope of this paper.

We hope that by pursuing a transparent approach, this work will contribute to an improved understanding of the various factors that determine the degree of agreement or disagreement between different simulations.

3 EARTHQUAKE SCENARIO

For this study, we selected the ShakeOut earthquake scenario, version 1.1. The ShakeOut is a hypothetical seismic event prepared by a multidisciplinary group from the U.S. Geological Survey (USGS), with the collaboration of SCEC and the California Geological Survey, and nearly 200 other partners from government, academia, the emergency response community and industry, who worked with the objective of identifying the physical, social and economic consequences of a major earthquake in southern California (Jones *et al.* 2008). Scientists from USGS and SCEC designed an earthquake of magnitude $M_{\mathrm{w}} = 7.8$ along the San Andreas fault affecting a region that includes all major populated areas

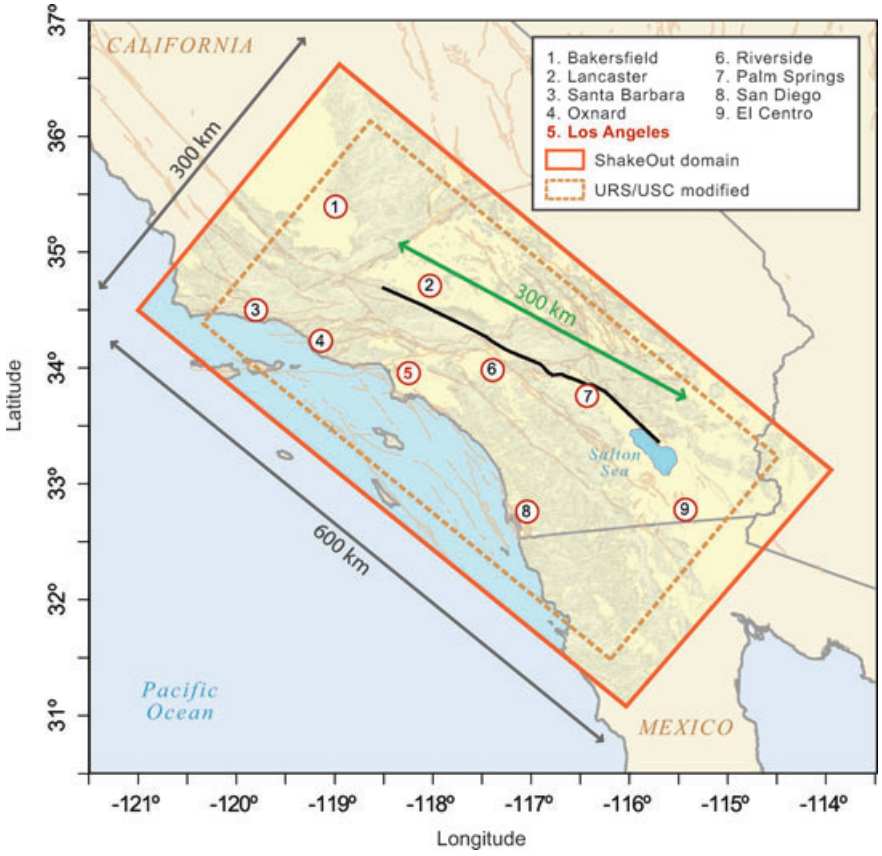

Figure 2. The ShakeOut earthquake scenario region, area of simulation, main cities within it and the fault-line surface projection. Grey shadowed areas represent the topography and light brown lines indicate quaternary faults in the region.

in southern California and Baja California, Mexico (Fig. 2). Initial results of the ShakeOut project may be found in Jones *et al.* (2008). Additionally, Graves *et al.* (2008) and Olsen *et al.* (2009) have reported USGS and SCEC ShakeOut-related estimates of ground motion broadband simulations and simulations with spontaneous rupture propagation, respectively.

Two fault rupture descriptions were prepared for the ShakeOut, versions 1.1 and 1.2. The difference between the two versions was the amount of slip heterogeneity at short length scales, which was increased in version 1.2. This means that version 1.2 used a rougher slip distribution and less coherent rupture front. Although such increase seemed to be a minor one, Jones *et al.* (2008) found it to have important implications in the study of the response of critical lifelines, especially at points where infrastructure crosses the fault. Thus, seismological and engineering analysis of the ShakeOut were done using simulation results from version 1.2. Because this paper focuses on model verification and not on the physical consequences of the simulation, and because only version 1.1 was simulated by all modelling groups, we limit our comparisons to results obtained using the initial rupture description—version 1.1. Figs 2–4 show the simulation domain—a rectangular box of 600 × 300 × 80 km—and the slip magnitude of the modelled fault, its rupture mode, and time progress.

To define the large-scale features of the slip distribution, end points, magnitude and rupture length, the USGS/SCEC team used geological slip rates for the San Andreas fault available from the Working Group on California Earthquake Probabilities, as well as palaeoseismic evidence for the dates of the most recent earthquakes. The rupture starts near Bombay Beach at Salton Sea at the southeastern end of the fault, continues near Palm Springs, and stops at Lake Hughes northwest of Lancaster (Fig. 2). The southeastern portion of the fault has not ruptured since approximately 1680 (Sieh 1986); thus the selection of Bombay Beach as the nucleation point. Selection of the northwestern endpoint was based on spatial variation of slip from the 1857 earthquake (Sieh 1978, 1986) and earlier events (Rust 2005), and also on the consideration that the extension was a determining factor for the magnitude and likelihood of the event—a longer fault rupture would have produced a larger but less common earthquake.

The slip along the fault was designed at two scales. First, the static rupture description, or background slip distribution, was defined for several portions of the fault; and second, a kinematic rupture description was modelled with a randomized variation of the average slip. The static rupture description was determined using a simple earthquake recurrence model in which the average amount of slip to be released would be the amount accumulated since the last event at study sites along each portion of the fault. This was calculated using estimates of fault dip, slip rate, date of last earthquake and seismogenic depth values from Wills *et al.* (2008). This background slip was used for the modelling of the kinematic rupture description, which was built upon the procedure used by Aagaard *et al.* (2008a) for simulating the 1906 San Francisco earthquake. The slip distribution and rake angles were randomized and the resultant spatial and temporal evolution of slip projected onto the non-planar 3-D fault geometry available in SCEC's Community Fault Model (CFM) triangular element representation. Each subfault was defined by the

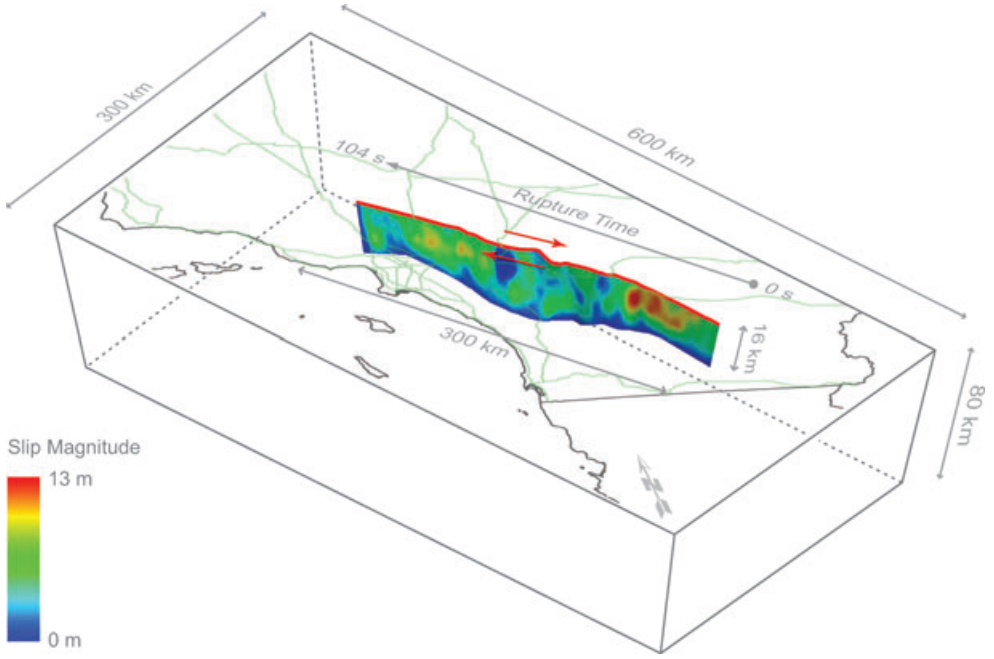

Figure 3. ShakeOut simulation fault and volume. Coloured surface indicates the slip magnitude along the fault. Rupture time signals the directivity of the event. Light-green lines denote the main interstate roads.

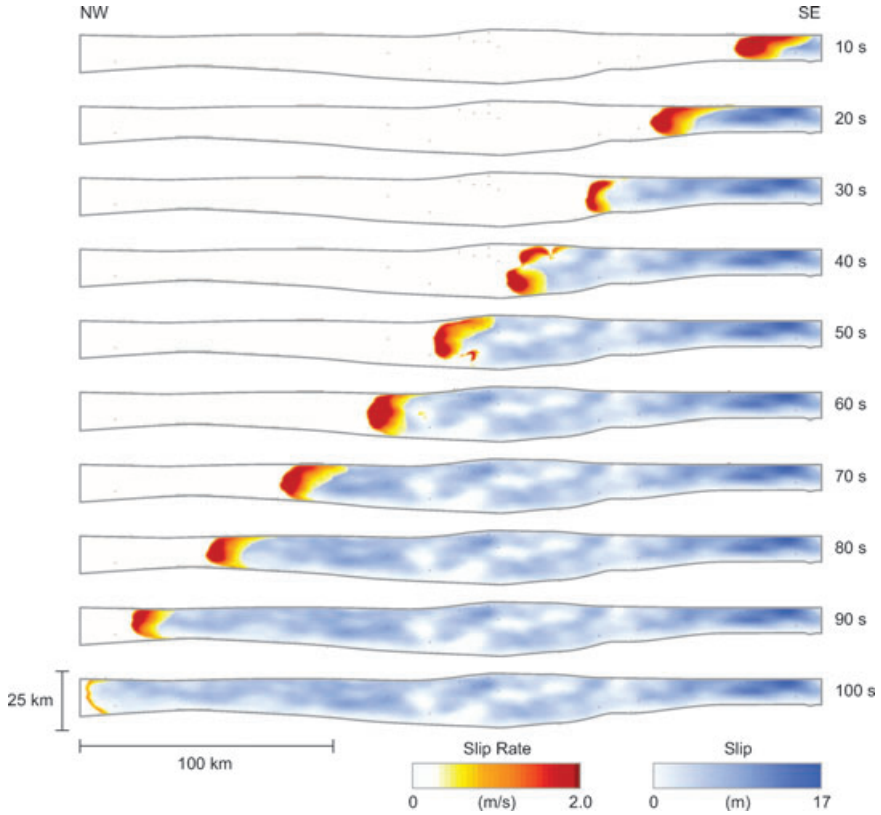

Figure 4. Time progress of the ShakeOut source description. Colourmaps denote the accumulated slip magnitude (blue) and the slip-rate (red) in the same vertical projection.

following parameters: slip time at which slip begins, slip vector, slip rate, rupture speed and subfault location (along strike and dip), and rise time. Figs 3 and 4 show the slip magnitude along the fault and the time evolution of the source. More details may be found in Jones *et al.* (2008, chapter 3).

4 MATERIAL MODEL

Material models, also called seismic velocity or crustal models, are a key element in the simulation process because, while being used to construct the mesh and determine the properties of mesh

elements that constitute the numerical representation of the system, their properties determine in good part the outcome of the simulation. High-resolution seismic velocity models in urban regions have received increased attention over the last decade due to the interest in earthquake modelling. Several material models have been developed and improved over the years for the regions of southern and northern California (e.g. Graves 1996b; Magistrale *et al.* 1996; Hauksson & Haase 1997; Magistrale *et al.* 2000; Kohler *et al.* 2003; Süss & Shaw 2003; Brocher 2005). We use a subset of SCEC's Community Velocity Model (CVM), version 4.0, in a discretized form that is stored in a database library called 'etree' (Tu *et al.* 2003); this accelerates considerably the mesh generation process (Schlosser *et al.* 2008).

The CVM was built upon the initial model assembled by Magistrale *et al.* (1996), and later extended and improved by Magistrale *et al.* (2000) and Kohler *et al.* (2003). In Magistrale *et al.* (2000), the *P*-wave velocity (V_p) of the major southern California basins (Los Angeles basin, Ventura basin, San Gabriel Valley, San Fernando Valley, Chino basin, San Bernardino Valley and the Salton Trough) was determined primarily by application of empirical rules based on depths and ages estimated for four geological horizons and calibrated for southern California with data from deep boreholes. The density and Poisson's ratio (and *S*-wave velocity, V_s) were estimated from V_p using empirical relationships. Outside and below the basins, properties were based on 3-D seismic tomography (Hauksson 2000). Kohler *et al.* (2003) added upper mantle seismic velocities to the model, based on the inversion of teleseismic traveltime residuals obtained from three temporary passive experiments and stations of the Southern California Seismic Network. The latest release by SCEC, CVM version 4.0, has a new San Bernardino Valley basement, based on recent inversions of gravity data confirmed by comparison to a seismic reflection line. The depth to basement of the Salton Trough was extended to the northern Mexican territory and redefined by a combination of seismic refraction surveys, inversion of gravity observations, surface geology, and boreholes. CVM version 4.0 also has a new V_p-density relationship based on density measurements from oil well samples in the Los Angeles basin and the San Gabriel Valley, geotechnical boreholes throughout southern California, and 12 oil wells along the Los Angeles Region Seismic Experiment lines.

The CVM is distributed as a Fortran code that reads points specified by latitude, longitude and depth, and writes out V_p, V_s, and density (ρ) values at those points. Since the Fortran code has to combine data from many different associated files, its performance for the construction of large meshes needed for FDM and FEM models is poor. To overcome this problem and to unify to the maximum possible extent the data used for the grids and mesh generation processes of each modelling group, we stored a discretized version of the CVM (for the region of interest) in an octant tree database form, called 'etree' (Tu *et al.* 2003). The etree library is known for its efficiency in query retrieval time and has been used successfully in past earthquake simulations (e.g. Akcelik *et al.* 2003; Rodgers *et al.* 2008). The discretization process, described in detail in Taborda *et al.* (2007), was done in a way that guarantees that the discretized version, hereafter called CVM–Etree, is appropriate for simulations up to a maximum frequency $f_{\max} = 1$ Hz and a minimum shear wave velocity $V_{s_{\min}} = 200\ \mathrm{m\,s^{-1}}$, with at least eight points per wavelength ($p = 8$). The resolution of the CVM-Etree decreases with depth while maintaining the rule $e_o \leq (V_s/f_{\max})/p$, where e_o is the octant edge size. This results in a minimum octant at the surface with $e_o = 18.3$ m—where there is maximum variability—and a maximum octant with $e_o = 9.2$ km at 80 km in depth—where the crustal structure is fairly homogeneous. Fig. 5 shows the southern California basins and other geological features as represented in the model, and the basins floor and shear wave velocity structure of the resulting CVM-Etree at various depths.

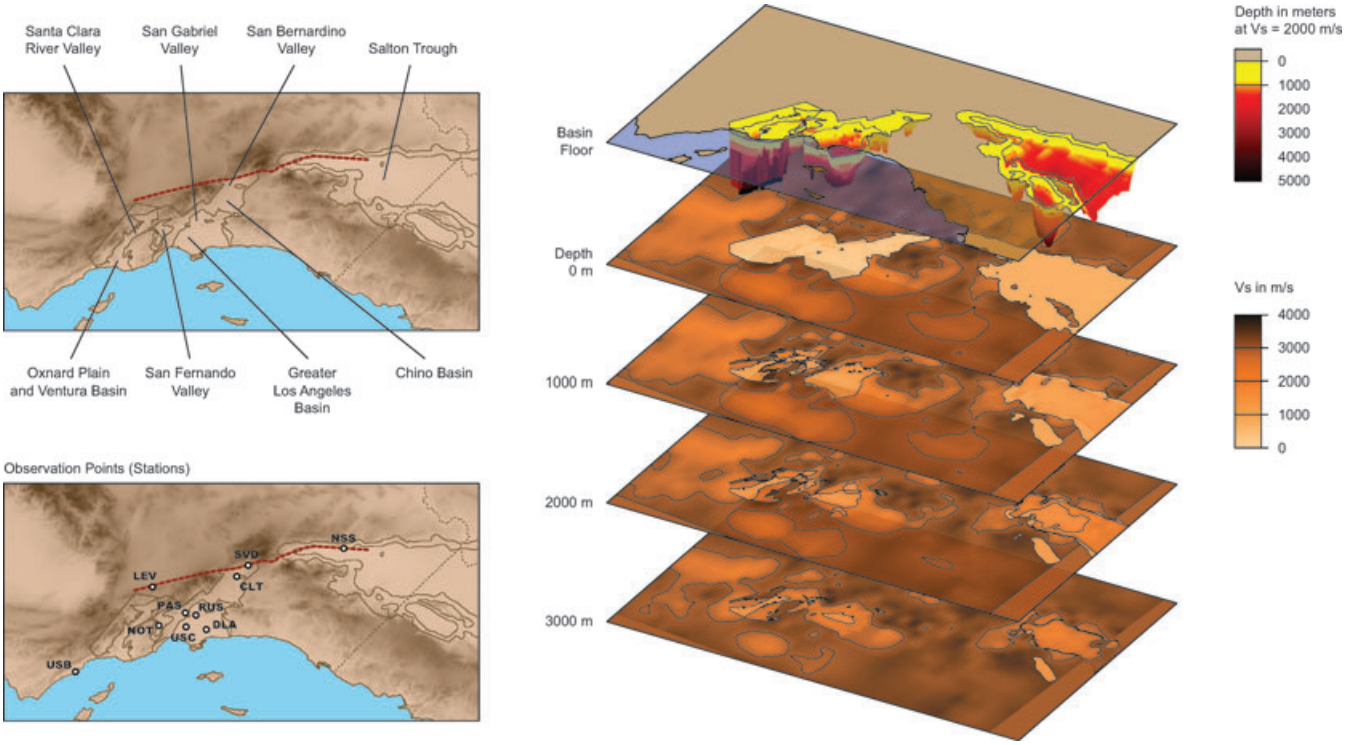

Figure 5. Southern California basins and other geological features (top left-hand panel), and basins floor and shear wave velocity structure (right-hand panel). Location of selected observation points (bottom left-hand panel).

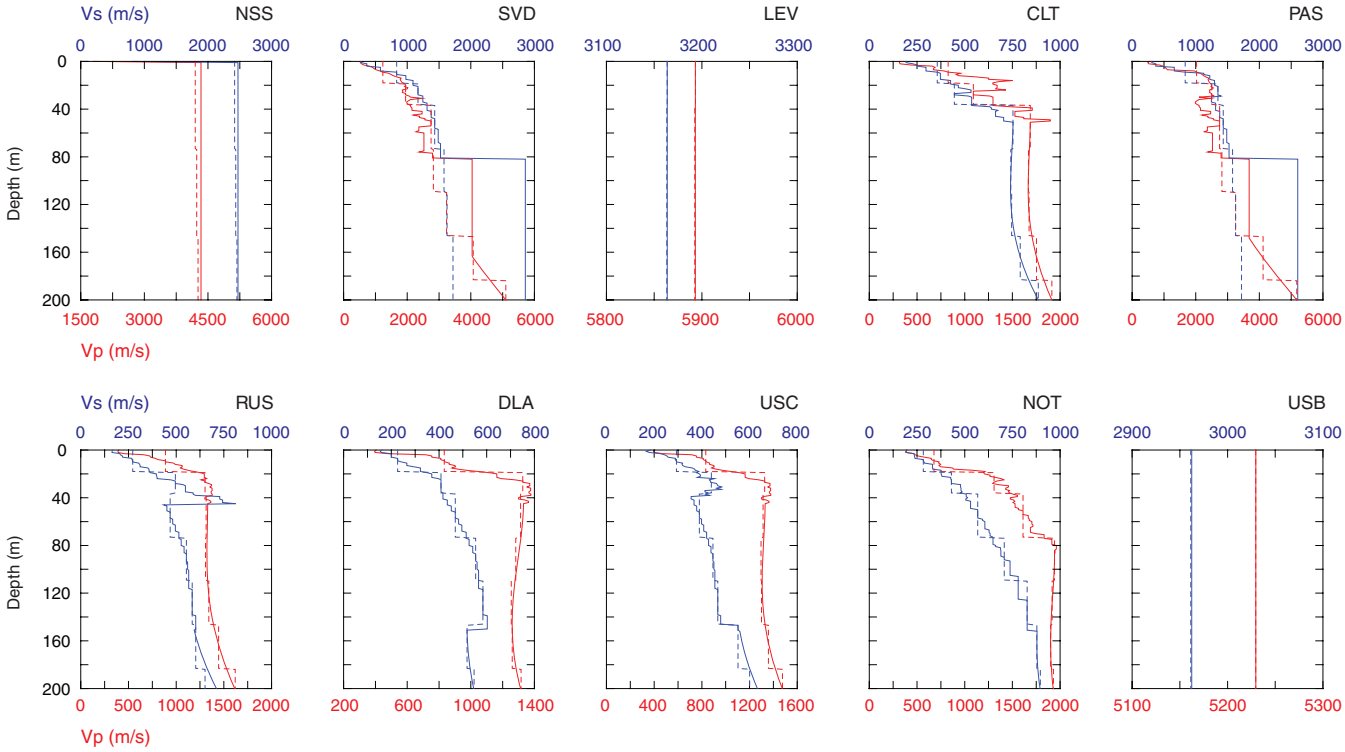

Figure 6. Soil profiles down to 200 m depth for selected locations throughout the region of interest (see Fig. 5). V_p profiles are shown in red, associated to the bottom axes. V_s profiles are shown in blue, associated to the top axes. Continuous lines represent values extracted directly from CVM version 4.0, while dashed lines correspond to the discretized CVM-Etree model.

Fig. 5 also includes the location of 10 observation points for future reference.

Figs 6 and 7 show V_p and V_s soil profiles for selected locations throughout the region of interest (see Fig. 5) for the first 200 m and 10 km in depth, respectively. Both figures include the profiles as extracted from the original CVM version 4.0 and the CVM-Etree. Differences between the original CVM version 4.0 and the CVM-Etree are of no significance to the simulation parameters (described in the following section) and, more importantly, to the objective of this study because, in the context of verification, what matters is to have the three simulation groups using the same velocity model, which in this case is the CVM-Etree. Nevertheless, despite all three groups using the CVM-Etree model for their simulations, this does not guarantee they will have exactly the same computational model, an aspect we will review later in the discussion of results.

5 COMPUTATIONAL METHODS AND IMPLEMENTATIONS

The simulation sets used in this study are the result of a modelling effort done by three independent research groups with the coordination of SCEC. Each of these groups has a solid background in earthquake simulations and has worked in previous similar exercises during the last decade, both independently and in collaboration with each other. Over this time, each group has developed its own implementation for solving the problem of anelastic wave propagation under seismic loading using numerical techniques on parallel computers. The first group, hereafter referred as CMU/PSC, solves the elastodynamics equations by means of a FEM approach. The other two, namely URS/USC and SDSU/SDSC, use a FDM approach. All three groups were given the same basic parameters for

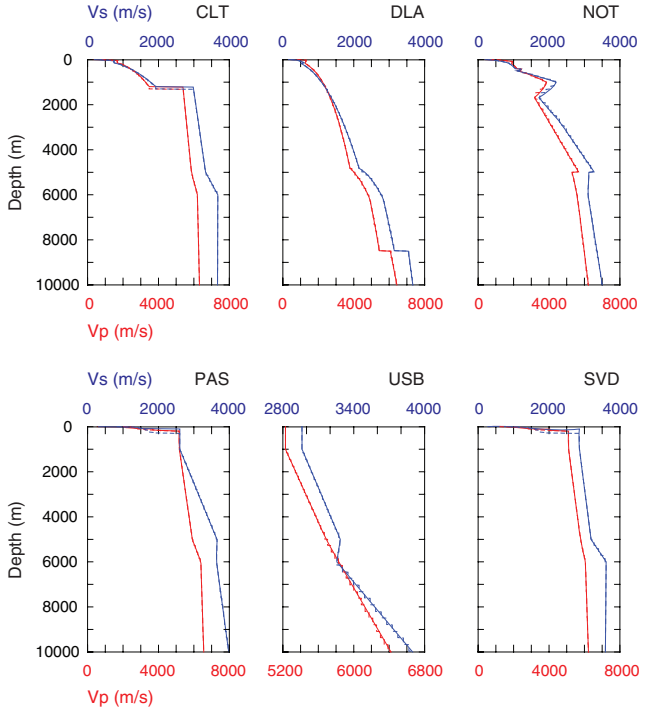

Figure 7. Soil profiles up to 10 km depth for selected locations (see Fig. 5). V_p profiles are shown in red, associated to the bottom axes. V_s profiles are shown in blue, associated to the top axes. Continuous lines represent values extracted directly from CVM version 4.0, while dashed lines correspond to the discretized CVM-Etree model.

Table 1. Domain and implementation characteristics of the three wave propagation codes.

	CMU/PSC	URS/USC	SDSU/SDSC
Domain[a]	Original	Modified	Original
Length (km)	600	500	600
Width (km)	300	250	300
Depth (km)	84	50	80
Southwest	−121.0000, 34.5000	−120.3578, 34.3985	−121.0000, 34.5000
Northwest	−118.9513, 36.6217	−118.6420, 36.1402	−118.9513, 36.6217
Northeast	−116.0323, 31.0829	−116.2349, 31.5472	−116.0323, 31.0829
Southeast	−113.9440, 33.1223	−114.4944, 33.2312	−113.9440, 33.1223
Projection	Bilinear	Spheroidal	Bilinear
Material model	CVM-Etree	CVM-Etree	CVM-Etree
Discretization	Octree-based FE	Staggered-grid FD	Staggered-grid FD
Space	Second order	Fourth order	Fourth order
Time	Second order	Second order	Second order
Resolution	Variable	200 m	100 m
$f_{\max}$ (Hz)	0.5	0.5	0.5
$V_{s_{\min}}$ (m/s)	500	500	500
Pts. per wavelength	$8 \leq p < 14$	5	10
Number of nodes	83 819 049	785 316 501	1806 304 901
Attenuation	Rayleigh	Coarse-grained	Coarse-grained
Q_s	–	$50V_s^b$	$50V_s^b$
Q_p	–	$2Q_s$	$2Q_s$
Q	$50V_s^b$	–	–
Absorbing boundaries	Lysmer–Kuhlemeyer	Clayton–Engquist	Perfectly matching layers

[a]The corners of the domains are given as longitude and latitude.
[b]V_s given in km s^{-1}.

the simulation: the source characteristics, and the CVM-Etree as the material model, plus an intrinsic attenuation description. Each ran its respective simulations with few departures from the prescribed conditions. This section explains each group's specific methodology and implementation, and describes the biggest differences between them. Table 1 summarizes this description.

The CMU/PSC simulation software is a FE parallel code, known as *Hercules* (Tu *et al.* 2006), that relies on an octree-based mesher and solves the elastic wave equations by approximating the spatial variability of the displacements and the time evolution with tri-linear elements and central differences, respectively. The resulting scheme has a quadratic convergence rate, in both time and space. The code uses a plane wave approximation of the absorbing boundary condition (Lysmer & Kuhlemeyer 1969), and introduces a Rayleigh attenuation mechanism in the bulk (Bielak *et al.* 1999). Rayleigh method does not distinguish between the *P*- and *S*-wave attenuation, but uses instead a single overall target quality factor Q, which for our calculations is set equal to Q_s. Since losses due to shear deformation are the most important, we consider this an acceptable adaptation. The traction-free boundary conditions at the free-surface are natural in the FEM. Thus, no special treatment is required (e.g. Bao *et al.* 1998). Hercules partitions the domain by recursively subdividing it into eight cubes (called octants) depending on the targeted *S*-wavelengths. This produces a non-conforming set of elements and nodes. The continuity of the displacement field is enforced by constraining linearly the motion of hanging nodes to anchored or independent ones. Once the mesh is distributed among the processors, the code obtains the equivalent time dependent forces of the double couples used to represent the source and proceeds to the displacements computation. Given that the elements share a scaled equivalent geometry, there is no need to store individual element mass and stiffness matrices. The solver computes displacements in an element-by-element fashion, scaling the stiffness and lumped-mass matrix-templates according to the material properties and octant edge-size (Bielak *et al.* 2005; Tu *et al.* 2006). This approach allows Hercules to considerably reduce memory requirements as compared to standard FEM implementations.

Both URS/USC and SDSU/SDSC groups use a staggered-grid FD technique that is fourth-order in spatial accuracy and second-order in temporal accuracy (Graves 1996a, 2008; Olsen 1994; Olsen *et al.* 1995b). Their codes rely on regular structured grids, which are built prior to the simulation. Both codes implement the same material parametrization, harmonic averaging of rigidity (μ) and arithmetic averaging of density (as described in Graves 1996a), but they differ in the specific location of the media parameters, which leads to somewhat distinct averaging schemes. However, both approaches have the same level of theoretical accuracy. To implement absorbing boundary conditions at the sides and bottom of the grid, URS/USC uses the paraxial approximation (type A1) proposed by Clayton & Engquist (1977), and SDSU/SDSC uses an implementation of perfectly matching layers as proposed in Meza-Fajardo & Papageorgiou (2008). In the case of the traction-free boundary condition at the free-surface, both groups use artificial planes above the surface that coincide with the location of either the normal, or the *xy* and *yz* stress nodes (Levander 1988; Graves 1996a; Gottschammer & Olsen 2001). Both groups include a coarse-grained implementation of the memory variables for a constant-Q solid to handle material intrinsic attenuation (Day & Bradley 2001), but they differ in that URS/USC also implements the improvements for very low Q proposed in Graves & Day (2003) which, among other aspects, include harmonic averaging of the moduli and Q, whereas SDSU/SDSC uses arithmetic averaging of the memory variables.

The numerical methods just described are those actually used in the codes tested for this study, and do not incorporate all of the most recent mathematical refinements that are known to improve accuracy in certain problem classes (see, e.g. Moczo *et al.* 2007, review). This limitation is a consequence of our focus on codes that are suitable for very large-scale applications. (Such codes undergo a high degree of algorithmic development, optimization and testing

to adapt them to high-concurrency computing systems, somewhat limiting the flexibility with which they can be adapted to rapid algorithmic evolution.) Among the methodological advances not tapped here but that have the potential to further improve accuracy, we note the Moczo *et al.* (2002) averaging scheme for heterogeneous material properties; improvements to the FD free-surface boundary accuracy by Kristek *et al.* (2002); Graves & Day (2003) improvement to the low-Q performance of coarse-grain memory-variable methodology that, while used in the URS/USC code, is not implemented in the SDSU/SDSC code (nor are additional memory-variable improvements by Kristek & Moczo 2003). Numerous other examples could be cited.

As mentioned above, all three groups used the CVM-Etree material model as the basis for constructing their corresponding mesh or grid. Because of computational limitations, the URS/USC group was restricted to simulating the scenario in a smaller domain of 500×250 km of area, and extending only 50 km deep (see Fig. 2), as opposed to the CMU/PSC and SDSU/SDSC groups, which targeted the original $600 \times 300 \times 80$ km volume domain, with CMU/PSC going slightly further in depth, down to 84.3 km, to satisfy their octree aspect-ratio rules. The maximum frequency of the simulation was set at 0.5 Hz and the minimum shear wave velocity set at 500 m s^{-1}. In the case of the FDM codes, this dictated a regular grid of 200 m, using five points per wavelength, as recommended by Levander (1988). URS/USC followed this rule. SDSU/SDSC, however, used a finer grid of 100 m with a corresponding minimum of 10 points per wavelength. This allowed us to examine the effect of the grid size on the ground motion, especially at stations distant from the fault. In the case of Hercules, the resulting mesh size is variable and depends on the tailoring of octants according to octree refinement rules (Bielak *et al.* 2005). The CMU/PSC group set the minimum requirement to be of at least eight points per wavelength, but the mesh generator in Hercules created elements as small as 73.2 m for soil deposits of $V_s = 500$ m s^{-1}, corresponding to up to 13.6 points per wavelength.

In all three cases, anelastic attenuation was modelled using prescribed relationships between the quality factor Q and the seismic velocity V_s at the element and nodal level for the FEM and FDM approaches, respectively. In the case of the URS/USC and SDSU/SDSC models, attenuation was independently assigned to S and P waves following the relations $Q_s = 50V_s$ and $Q_p = 2Q_s$, where values of V_s are given in kilometres per second. This Q model has been used successfully for previous earthquake simulations in the Los Angeles basin region (Graves & Pitarka 2004; Graves 2008). On the other hand, because its current implementation does not explicitly separate S from P waves, CMU/PSC used a global value of $Q = 50V_s$. The effects of these and other differences intrinsic to the implementations of the three groups are the subject of the following sections.

6 RESULTS AND COMPARISONS

A common first step in a verification process is a graphical comparison of results. More in-depth verification requires the use of metrics to allow one to quantify the level of agreement between the results being compared. In this section we evaluate our results both qualitatively and quantitatively from (i) a regional perspective and (ii) a local perspective. We limit the first part to qualitative (graphical) comparisons of the results over the entire region. In the second part, we do both qualitative and quantitative comparisons at ten selected locations. By quantitative comparisons we mean the verification of the three simulation sets by means of two different criteria: the misfit criteria proposed by Kristekova *et al.* (2006) and the goodness-of-fit scores introduced by Anderson (2004). Both methods are designed to quantify the level of agreement between two signals. The first uses a continuous wavelet transform analysis to compare two signals in the time, frequency and time-frequency domains, while the second uses a collection of engineering and signal-processing parameters to evaluate the overall agreement between them.

6.1 Regional perspective

The first step in our comparison is qualitative and graphical. Later on we introduce quantitative comparisons. Fig. 8 shows snapshots at different times of the magnitude of the horizontal velocity at the free surface, calculated as the square root of the sum of squares of the two horizontal components, for the three groups. Although smaller and larger values are present in the results, the colour limits in the figure were set to 0.05 and 2.0 m s^{-1} for visual convenience. Other than the differences resulting from URS/USC using a smaller domain, all triplets are in good agreement with each other at all times. Discrepancies are practically unnoticeable unless one zooms in and examines the triplets carefully. Those small differences are more visible in wave fronts with amplitudes close to the lower limit of the colour scale. See, for example, the wave at the lower left-hand side behind the main wave front. Still, on a first, visual comparison, these differences appear quite small.

Fig. 9 shows a similar comparison for the accumulated peak ground velocity (PGV) and displacement (PGD). In both cases one sees a very good agreement in the general distribution of peak values throughout the region and in areas of importance like the greater Los Angeles basin, the San Fernando valley, and the Oxnard plain and Santa Clara river valley (see Fig. 5 for reference). The same can be said about the peak values distribution along the fault and areas nearby, especially in the peak velocity triplet. Differences here, though, are more noticeable, especially in the case of the PGD triplet in the areas of the San Diego and Imperial counties. These differences, however, are close to the lower limit of the colour scale and, thus, it is difficult to say at this point, if they reflect that particular choice. This is in fact a problem that would either remain, be translated to other areas, worsen, or be artificially hidden, depending on the selection of a different colour scale. This is an intrinsic limitation of graphical comparisons of this kind and one that is not usually discussed or backed with a more thorough verification.

6.2 Local perspective

Even though the regional perspective helps ensure that the basics of the scenario are correctly represented by each simulation group, and a regional comparison is also a good way to do a first evaluation of the level of agreement between the different sets, it is not sufficient. A more detailed comparison is necessary by looking at results at individual locations.

6.2.1 Graphical verification

Fig. 10 shows the particle velocity at the free surface of selected points, or stations, spread throughout the region (see Fig. 5). It is worth observing that it took us several iterations to arrive at these results. The initial discrepancies were somewhat larger due to differences in the implementation of attenuation models, the mesh and grids material properties, and in the number of source points used to define the source rupture kinematics. Having reached agreement on the necessary parameters (e.g. using a common representation of

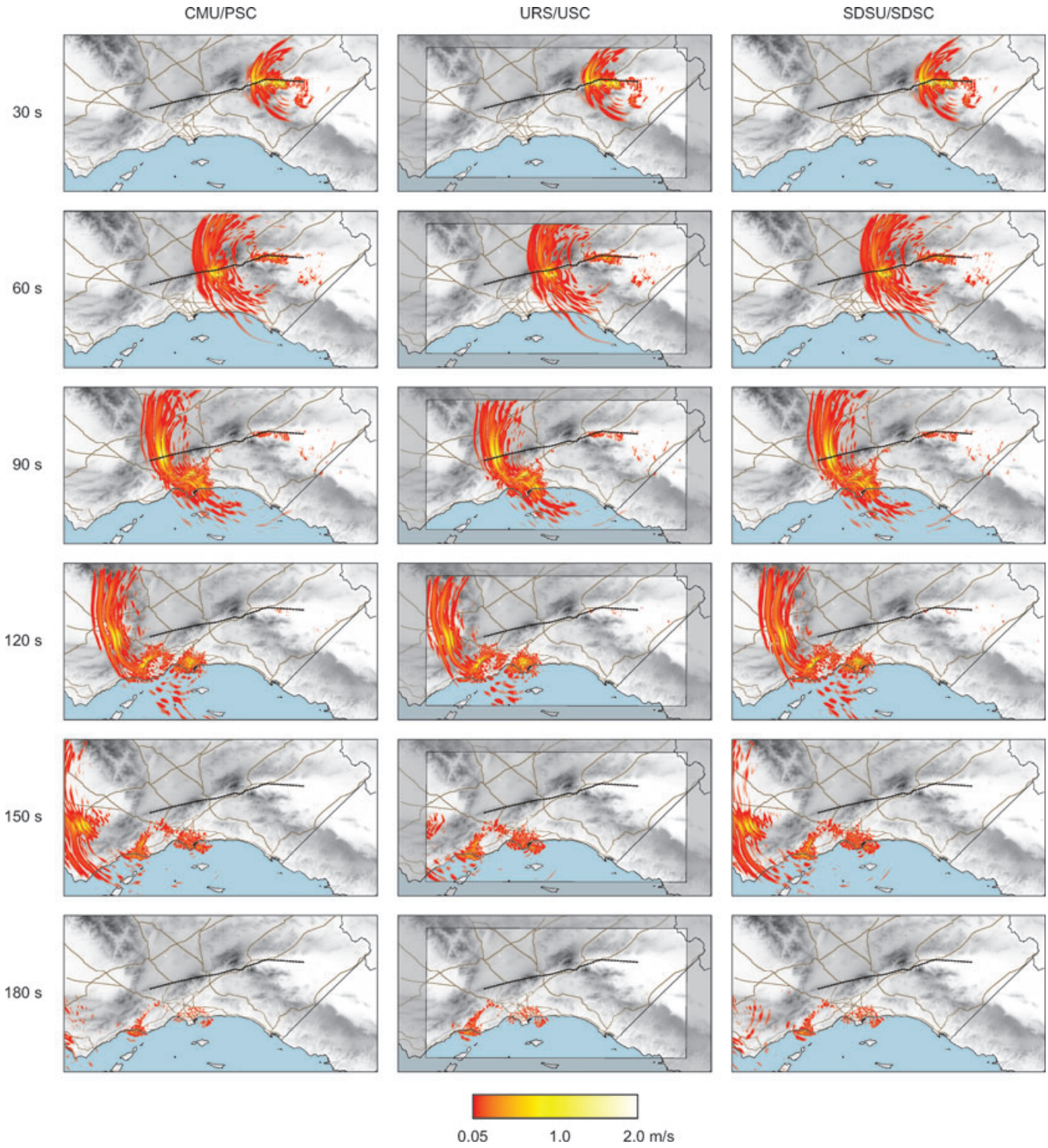

Figure 8. Snapshots of surface horizontal magnitude velocity for the three simulation sets at different times.

the material model, setting an appropriate number of source points per wavelength), we expect that no iterations will be required for future simulations with different source rupture or material models.

The similarities between each triplet for all the stations and components of motion observed in Fig. 10, underscore the good level of agreement achieved by the three groups. Nevertheless, slight differences are noticeable over time, and in the peak values of each set, shown at the right-hand side of each triplet. Differences in the peak values are somewhat more prominent at stations near the fault (SVD, LEV), while differences in phase are more noticeable for the surface waves at stations on softer soils (DLA, USC and NOT), or farther from the fault (USB). We believe the misfits to be mainly due to two types of error. A numerical solution is subject to error both from the discretization of the dynamic field variables (e.g. truncating their basis-function expansions in the FEM or truncating the representation of their derivatives in the FDM), and from the discretization

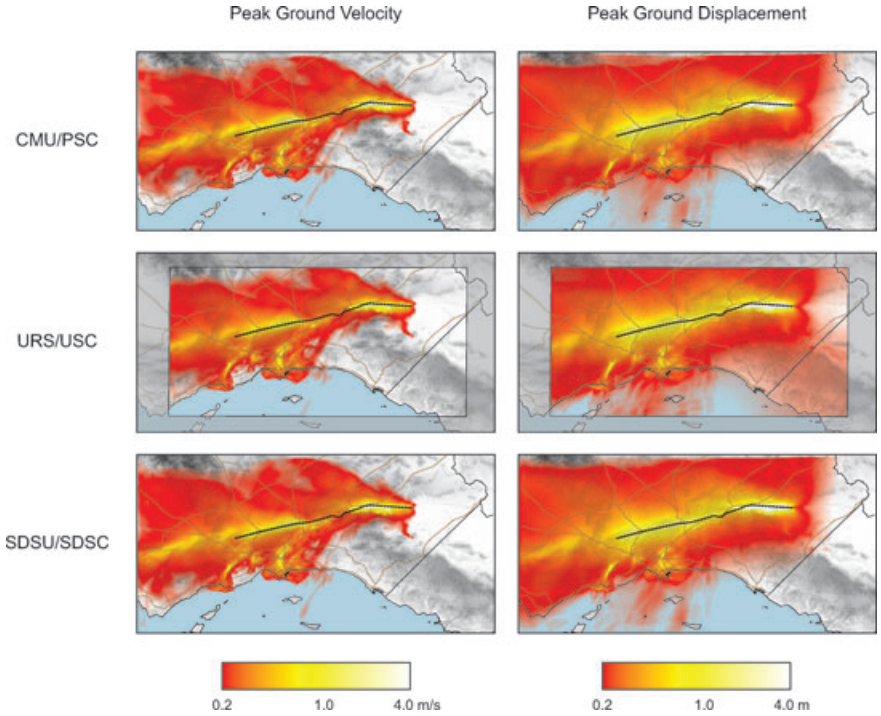

Figure 9. Horizontal peak ground velocities and displacements throughout the region.

of the material properties. In our case, the latter may dominate the former. We will discuss the effects of these errors in greater detail later. For now, it suffices to say that late arrivals or surface waves seem to be faster for CMU/PSC, followed by SDSU/SDSC and then by URS/USC results. Amplitudes do not show a definitive trend, although SDSU/SDSC tends to produce higher values.

An important aspect of synthetics comparisons is to check the arrival time of waves. Fig. 11 shows cumulative energy functions for each station triplet calculated as

$$E(t) = \int_0^t v^2(t)\mathrm{d}t,$$

where v is velocity. For each frame in the figure, the energy traces are normalized with respect to the largest final energy of the three synthetics—the value shown at the top right-hand side of each frame. This comparison may seem of limited utility due to the cumulative nature of the error over time. However, when it comes down to comparing arrival times, it is much clearer here than in the time traces—not just for the first arrival but also for subsequent ones. In both figures, the stations have been ordered with respect to their distance to the fault. One can clearly see that in all cases the arrival time of each triplet is coincident. This is true not only for signals with sharp steep energy traces like PAS or RUS, but also for locations where energy arrives in multiple bursts, like DLA and USC. This is also true for observation points sitting right on top of the fault (NSS, SVD and LEV), as well as for the farthest of all (USB). Despite the reasons stated above about this being somewhat an unfair comparison, we see quite a good level of agreement between most of the triplets.

When making this kind of verification it is very important to contrast the frequency content distribution of signals. Fig. 12 shows comparisons of all stations and components of motion for amplitude of the Fourier spectra of the synthetic triplets. Again, the similarities in each triplet are greater than the discrepancies; not that the latter passed unnoticed. Peaks and troughs are very close, though with some substantial differences at various locations and frequency ranges for different components. For instance, at various locations such as NSS, LEV and RUS, the amplitude at the higher end of the spectra tends to be smaller for the URS/USC simulation. This may be a consequence of the lower number of points per wavelength used by URS/USC in comparison to the other two groups. Nevertheless, broadly speaking, all triplets have the same general shape.

6.2.2 *Quantitative verification*

To gain a better sense of the differences and similarities between the various simulation sets, we now take verification to a quantitative level. For this we use (i) the misfit criteria proposed by Kristekova *et al.* (2006) and (ii) the goodness-of-fit criterion by Anderson (2004). The former measures the level of disagreement or misfit between two signals in a time-frequency fashion in two respects, the envelope misfit and the phase misfit. It does so by means of a continuous wavelet transform that can ultimately be summarized in single-value measures of the misfits. The latter evaluates the level of similarity or goodness-of-fit between two signals by applying to them ten different comparison metrics, each producing a final score. Results are summarized by averaging the scores in a per frequency-band and broadband basis over all ten metrics.

While the two criteria target similar aspects of signals, we have not found any clear correlation between them. It could be argued that the mathematical nature of the approach taken by (Kristekova *et al.* 2006) makes their criteria more appropriate for verification studies; and that the somewhat more practical and tangible method proposed by (Anderson 2004), conceived from an engineering viewpoint, is better suited for validation purposes. Without any clear reason to prefer one over the other, or limit their use to either kind of study,

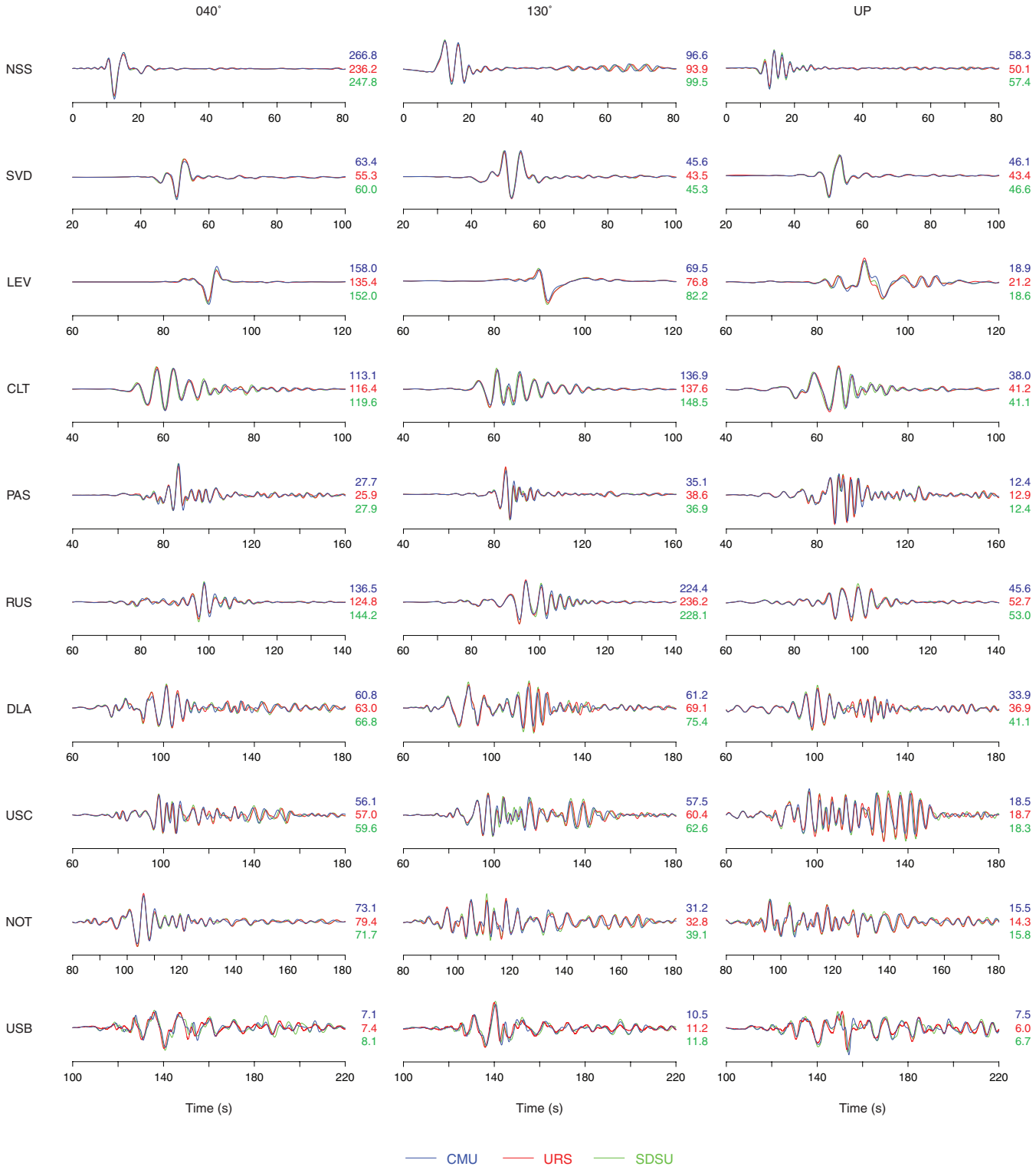

Figure 10. Particle velocity for the selected stations in each direction of motion. Peak values are shown on the right-hand side of each trace for the three simulation sets—in cm s^{-1}. Total durations were chosen for each station to include only the intense phase of motion and facilitate the visual comparison. Stations are ordered according to the distance from the fault, the top three being the closest, and the bottom one being the farthest.

we felt that computing both criteria would be the best course, and perhaps serve as springboard for further research.

6.2.2.1 Misfit criteria. The core of the misfit criteria proposed by Kristekova *et al.* (2006) is the time-frequency envelope and phase misfit functions, or TFEM and TFPM, for short, that characterize the level of misfit between two signals for each point in time and frequency, based on the time-frequency representation of the signals obtained from the continuous wavelet transform using

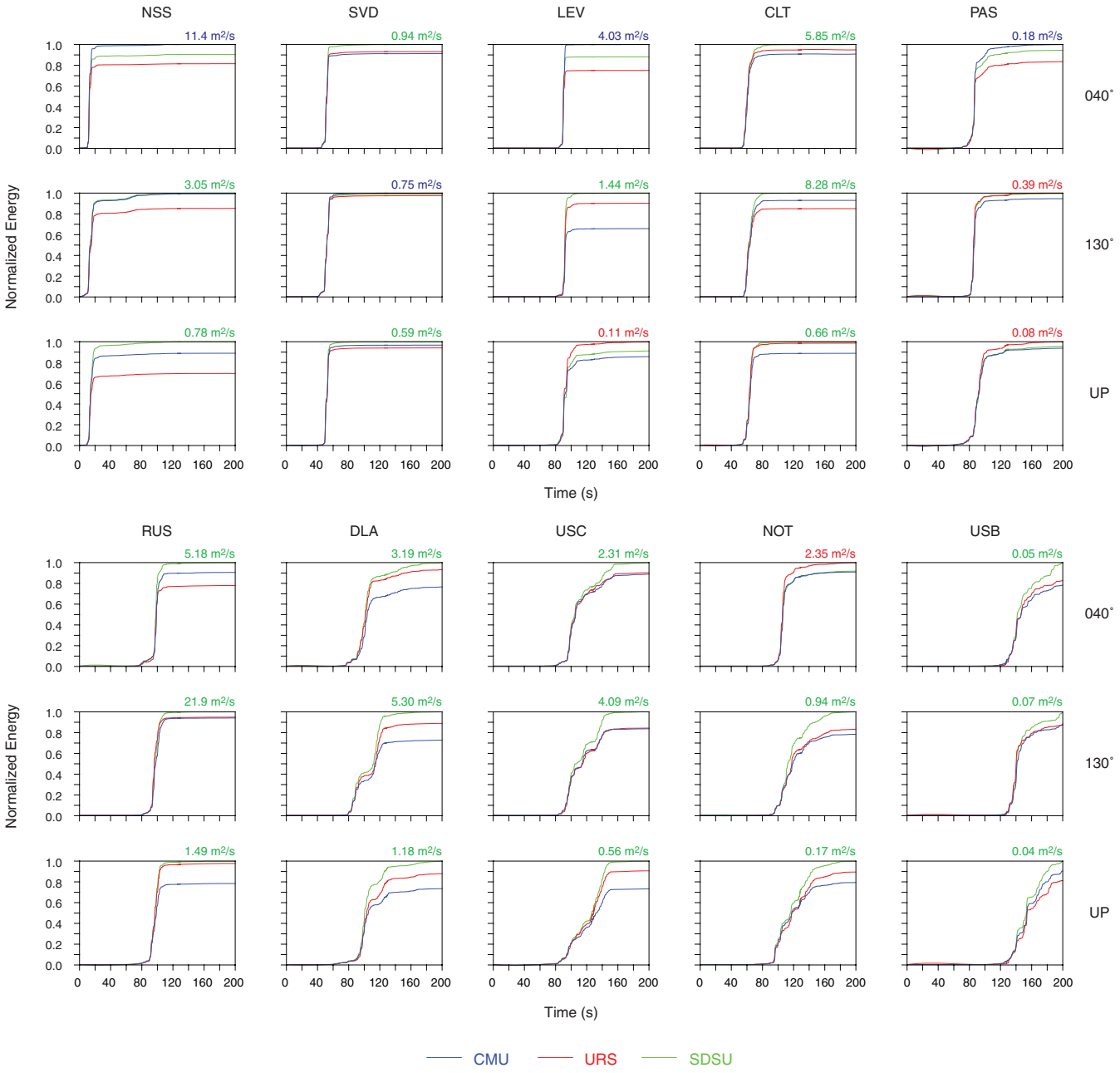

Figure 11. Comparison of energy time functions for the selected locations. Each station set is normalized with respect to the higher value of the three, and the value is shown at the top of each frame. The font colour of the maximum is associated to the corresponding simulation set.

the Morlet wavelet. Kristekova *et al.* also introduced measures derived from TFEM and TFPM to have the misfit measured only in time or frequency—as projections of the time-frequency functions over the preferred domain. Ultimately, by integration over time and frequency, TFEM and TFPM can also be reduced to single-value measures of the misfit, EM and PM for the envelope and phase misfits, respectively. The value of the misfit at the given point in time and frequency varies from 0 to 1, 0 representing no misfit or a perfect match between the signals, and 1 representing a 100 per cent difference between them with respect to the maximum value of the two.

Fig. 13 shows the results of applying both TFEM and TFPM at four selected locations of the simulation for one component of motion (130°). Because the comparison must be done in pairs, we applied the criteria for the possible combinations of the three simulation groups. The single value misfits (EM, PM) are also shown in the figure near the bottom right-hand corner of each time-frequency frame. In all cases we observe that the misfit spread is concentrated throughout the intense phase of the signals, with a tendency to concentrate towards frequencies higher than 0.1 Hz. Note that no discrepancies are observed at lower frequencies. This may be taken as an indication that, the finiteness of the simulation's domain and the different accuracy of the absorbing boundary conditions used by each group (boundaries which are located sufficiently far away from the fault), and the different behaviour of each group's intrinsic attenuation models at low frequencies, do not appear to impose a lower frequency limit to the simulation. That the absorbing boundaries do not seem to play an important role on

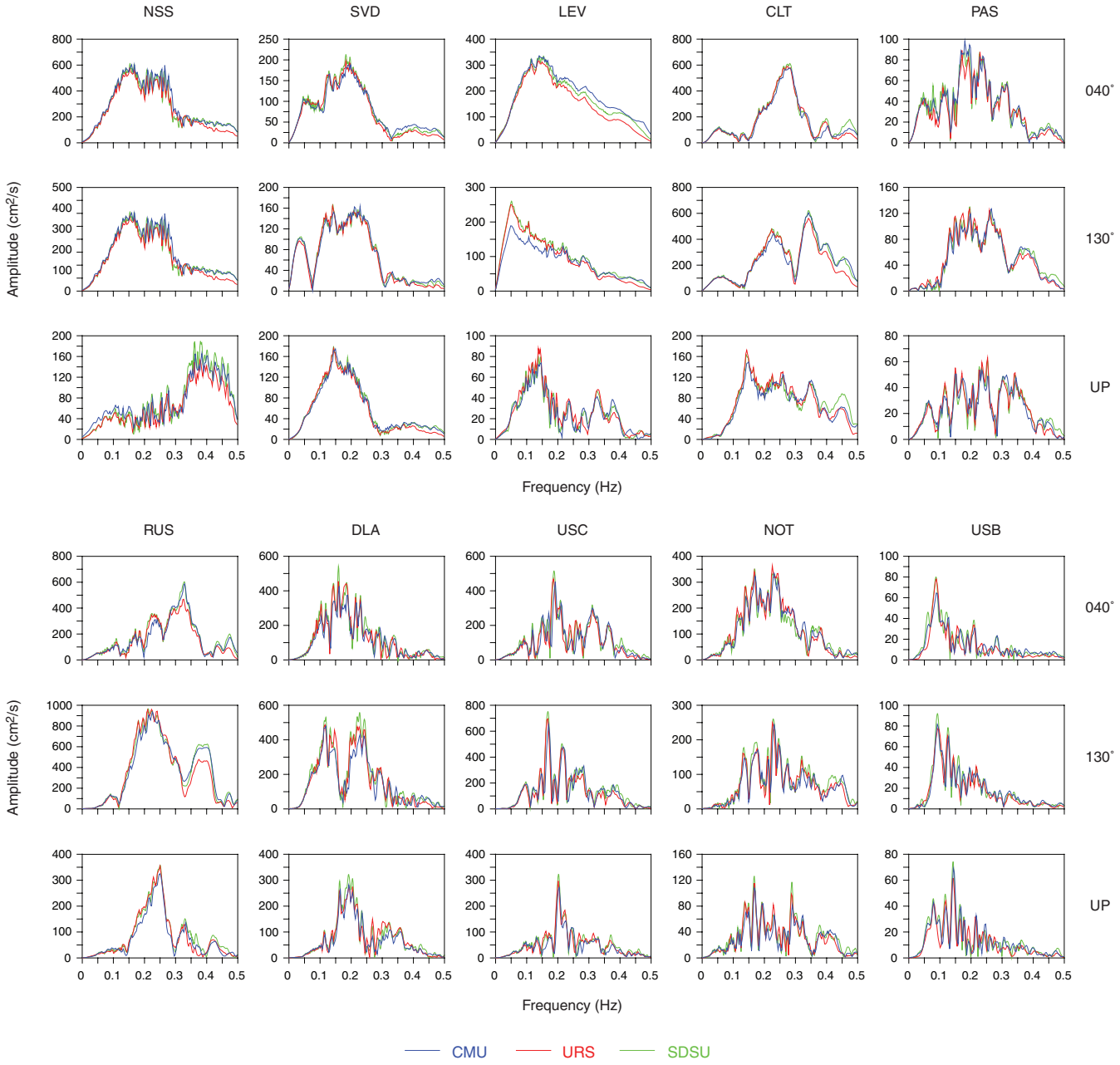

Figure 12. Comparison of Fourier amplitude spectra of velocities for each station in the components of motion.

the ground motion in the most highly populated regions, west of the San Andreas fault, can be seen in Fig. 9, especially in the right-hand panels for the PGD.

Although this full comparison of TFEM and TFPM allows one to see where the differences are in the time-frequency space, presenting this level of detail for each component at all 10 selected locations seems unnecessary. We rather focus on the single value misfits, EM and PM, which, as seen from Fig. 13, provide a good overall measure of the misfit of a given pair.

Fig. 14 shows the single-value EM and PM scores for each component of motion at each selected location. Each criterion is applied to each pair of simulation sets. The average values of the three comparison pairs for each location are shown at the top of each frame, and the averages over all locations for each pair of sets is shown to the right-hand side. The values at the top right-hand corner are the global average misfit for that particular criterion and component of motion. In all cases, the phase misfit is smaller than the envelope misfit by a margin of about 0.10. In general, individual values and local averages do not exceed 0.30 and 0.20 for EM and PM values, respectively. In terms of global averages, EM and PM values do not exceed 0.20 and 0.10, respectively. Fig. 15 summarizes the results of the misfit analysis by averaging the results for all components of motion and pair sets to give a final value of EM and PM for each selected location. We observe that with the exception of LEV (for EM), stations closer to the fault (NSS, SVD and CLT) show lower misfits than those far from the fault (USB) or on softer soils (DLA, RUS and USC).

We believe that the ceiling marks of 0.30 and 0.20 for EM and PM constitute valid reference values to determine a good level of agreement for our particular application. These ceiling marks were

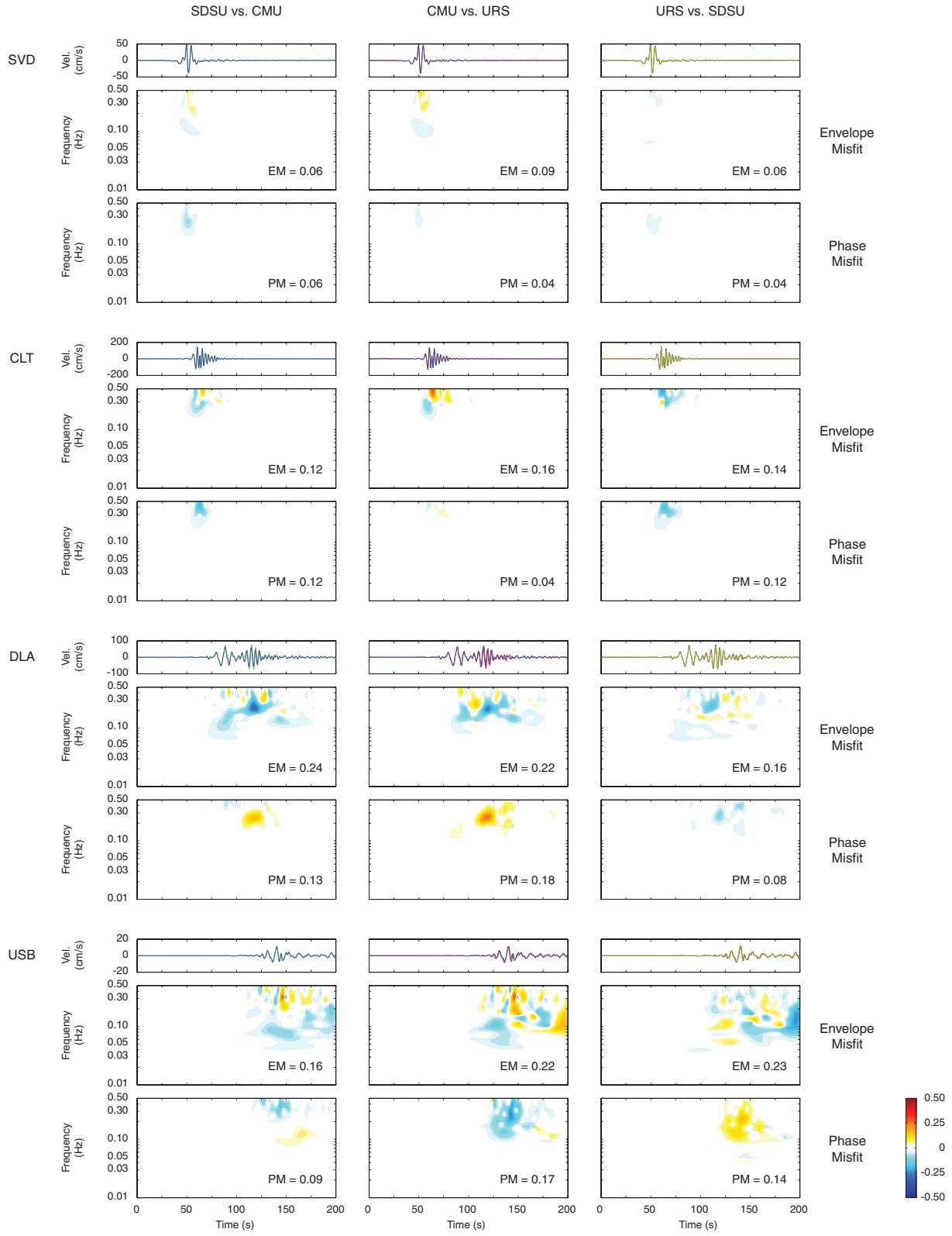

Figure 13. Results of the time-frequency envelope (TFEM) and phase (TFPM) misfit criteria proposed by Kristekova *et al.* (2006) for the velocity signals for the 130° component of motion at four selected locations in the simulation. The misfits are presented by pairs for the three possible combinations among the three simulation groups. Each frame also contains its corresponding single-value misfit.

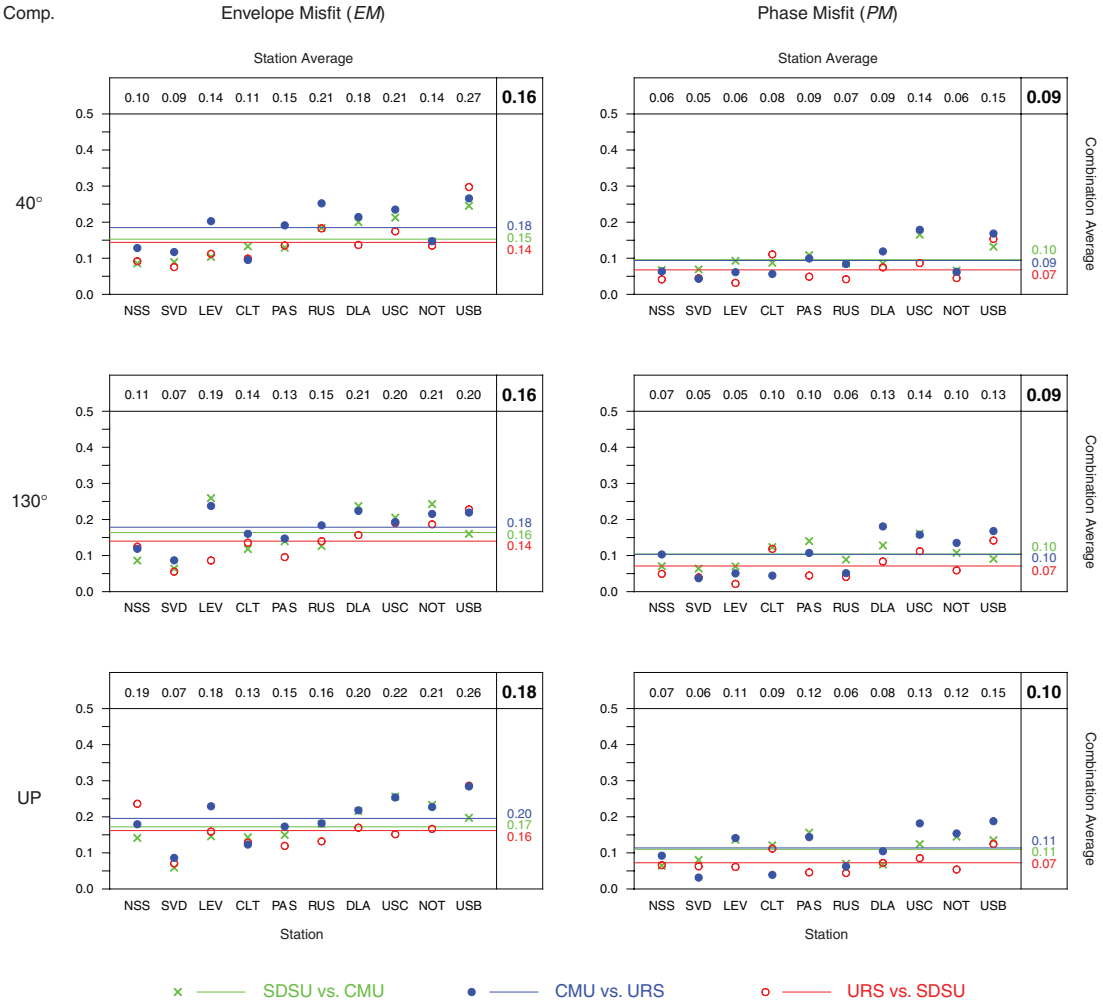

Figure 14. Results of the envelope and phase misfit criteria (Kristekova *et al.* 2006) for the three components of motion. The criteria were applied in pairs combining all three simulation sets for the selected stations. Averages of the three combinations for each station are shown at the top of each frame, and average of all stations for each combination at the right-hand side. The top right-hand corner indicates overall average misfit value for each particular component-misfit combination.

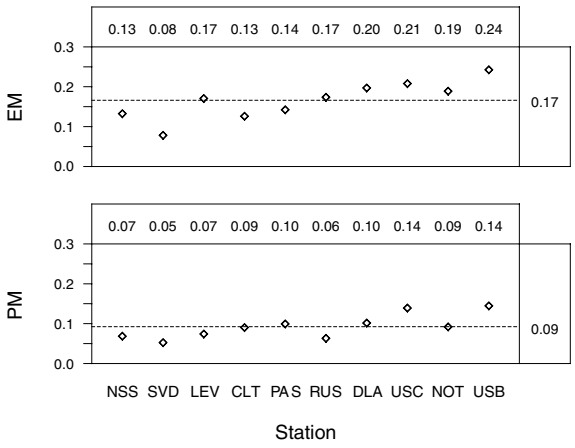

Figure 15. Summary of results for the misfit criteria obtained by averaging the values of all comparison pairs and components of motion for each selected location. The values at the top are the averages of the three simulations for each location, and the values on the right-hand margin give the final average over all selected locations, for each criterion EM and PM.

set based on the 'worst' misfit values, both observed at the USB comparisons, where $EM_{max} = 0.30$ and $PM_{max} = 0.19$. Yet, considering the distance of USB from the rupture zone and the complexity of the rupture and the velocity model themselves, we think that, from the graphical comparison at the bottom triplet of Fig. 10 and its corresponding spectra in Fig. 12, together with their misfit values and time-frequency comparison (bottom panel of Fig. 13), the sets compare rather well. For instance, the fractional misfits in peak velocity at USB are all less than 21 per cent, peak velocity arrival time misfits are all less than 18 per cent, phase differences in the latest-arriving Rayleigh wave packet are less than $9\Delta t$, and Fourier amplitudes smoothed over bandwidth 0.1–0.4 Hz disagree by less than 30 per cent. Therefore, these ceiling marks are acceptable to claim that any EM < 0.30 and PM < 0.20 constitutes a good comparison.

6.2.2.2 Goodness-of-fit criteria. Although we consider the claim above to be valid, it still depends on our subjective judgement of the values obtained by the misfit criteria linked to our observation of the graphical comparison. It is worthwhile to reinforce our interpretation of the results with additional metrics of comparison—metrics conveying more physical meaning to seismologists and engineers. To this end we turn to the goodness-of-fit criterion proposed by

Anderson (2004). This criterion evaluates the similarity between two signals by comparing them with ten different metrics (C*i*). Each parameter is scaled such that it yields a score between 0 and 10, where a score of 10 corresponds to a perfect match between the two signals for the given metrics. The ten metrics are: Arias duration (C1), energy duration (C2), Arias intensity (C3), energy integral (C4), peak acceleration (C5), peak velocity (C6), peak displacement (C7), response spectrum (C8), Fourier amplitude spectrum (C9) and cross correlation (C10).

All these parameters have a physical meaning in earthquake engineering and/or seismology, and an interpretation in signal processing. The scoring process is done for each parameter individually and a final score is obtained by averaging all ten scores, $S = (\sum_1^{10} Ci)/10$. Anderson proposes to do the respective operations over prescribed frequency bands and over the entire bandwidth of the signals, each resulting in an independent score. This results in three different forms of presenting the final scores: (i) those of each frequency band evaluated individually, SB*i*, where *i* is the band identifier; (ii) a score corresponding to the analysis over the entire broadband of the signal, S2 and (iii) a final score that corresponds to the average of the scores of each frequency band and that of the complete broadband, $S1 = (S2 + \sum_1^n SBi)/(n + 1)$, where *n* is the number of bands considered. According to Anderson, S1 more fairly represents the quality of the comparison.

Fig. 16 shows the scores of the comparisons for the per-band analysis (SB*i*), the broadband (S2) and the final average (S1) for the 10 selected locations in each component of motion. The comparisons, as before, were done in pairs of simulation sets. Averages of the three pairs for each station are shown in the top margins and the average over all locations in the right-hand margins. The

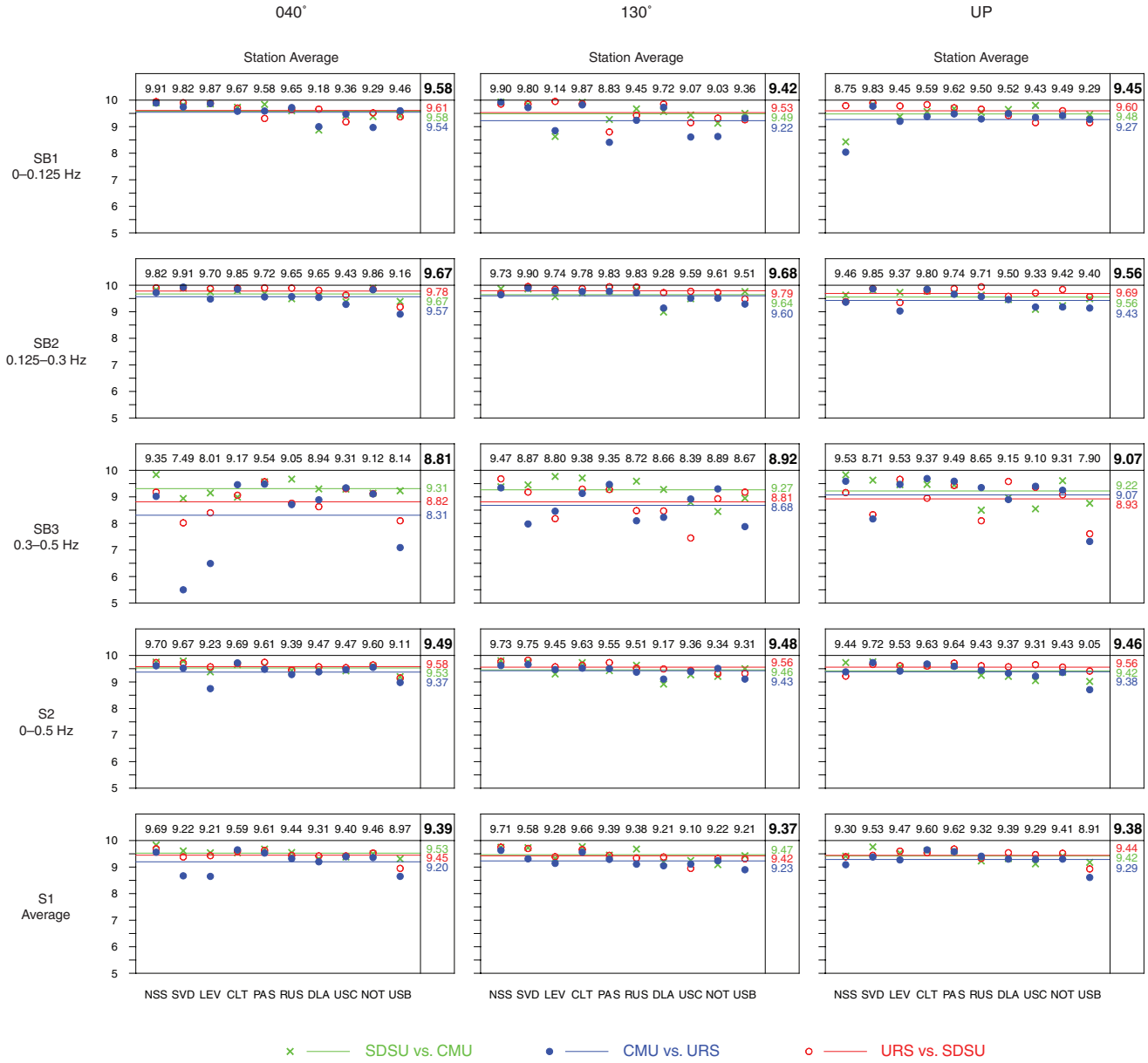

Figure 16. Goodness-of-fit scores (Anderson 2004) for each of the frequency bands considered (SB*i*), the broadband (S2) and total average (S1) for each station and in each motion component. Averages for each station are shown on top of each frame and averages of each set combination on the right-hand side. The top right-hand corner values are overall averages for each criteria.

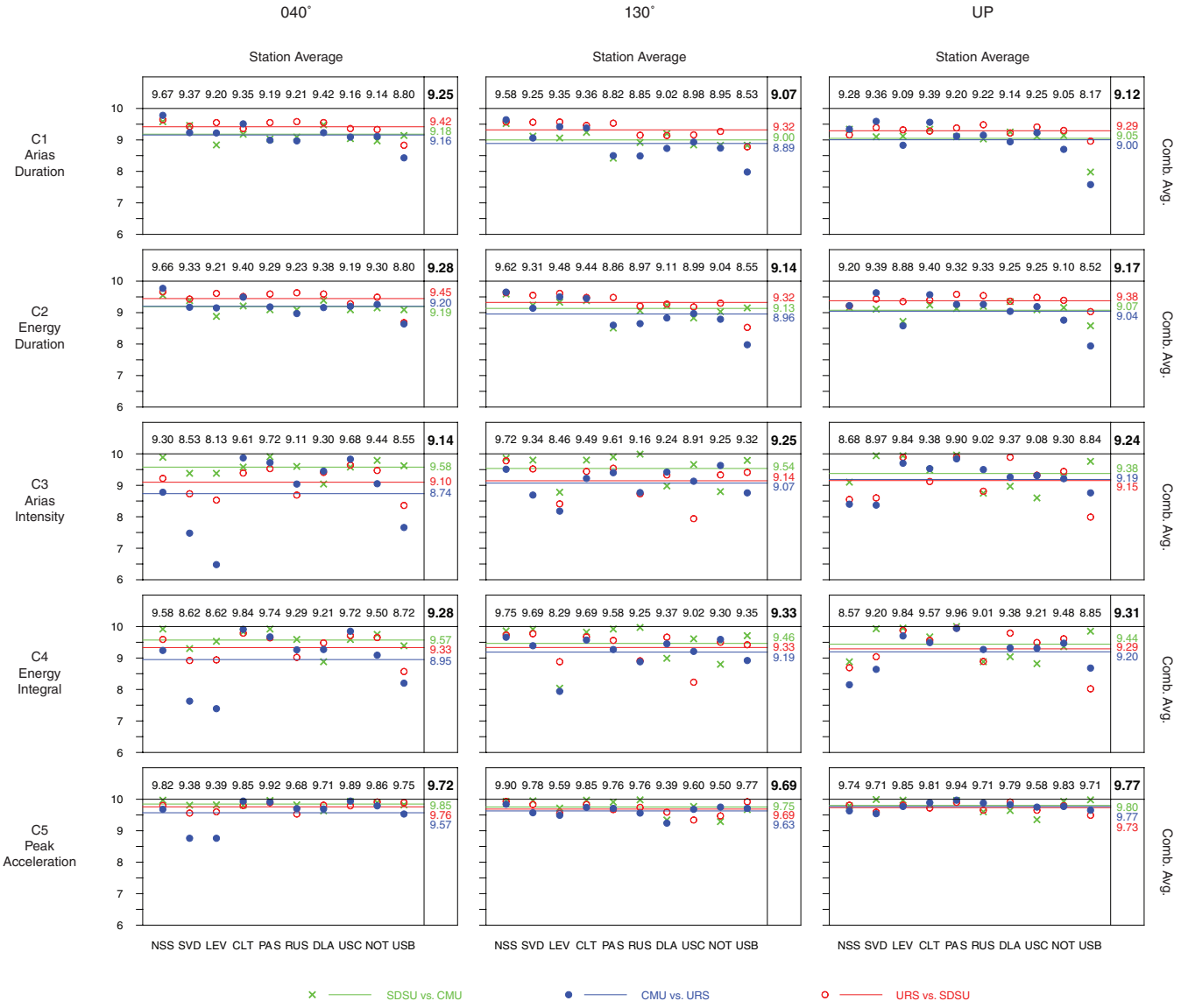

Figure 17. Results of the goodness-of-fit scores for the ten parameters proposed by Anderson (2004) for each station, in each component of motion, applied by pairs of simulation sets. The averages for each station are shown at the top of each frame. The values in the right-hand margins give the averages of each combination pair. The top right-hand corner values are overall averages for each criterion.

top right-hand corner values represent global averages of each case. For the analysis of band filtered sets we chose the following three pass bands: 0–0.125 Hz (SB1), 0.125–0.3 Hz (SB2) and 0.3–0.5 Hz (SB3). Although Anderson suggests to do a different subdivision—one whose spacing is approximately logarithmic, we adopted these bands from the shape of different spectra in Fig. 12, where we identified some signals showing well defined troughs around these frequencies.

With isolated exceptions (from SB3), all comparisons for the frequency band results score above 8. According to Anderson's calibration, were the comparison carried out against observations, a value higher than 8 ought to be regarded as an 'excellent fit'. For the broadband analysis (S2) all values are larger than 8.5 and a large majority is above 9. The same happens for the final score (S1), and if one is to focus on the averages by individual pair comparisons, that is, the values on the top margins of the S1 frames, all scores are greater than 9.1 with the sole exception of signals at USB in the 040° and UP components, which are still rather high (>8.9). We explain the lower and more scattered scores in SB3 (0.3–0.5 Hz), as a result of this frequency band having less energy content than SB1 and SB2 (0–0.3 Hz), especially in the case of SVD and LEV (040° and 130°), USC (130°) and USB. Nevertheless, a majority of SB3 scores is still high ($\gtrsim$8).

Because each score is the result of averaging the individual scores of the above mentioned parameters, one can equally do the average over the pass bands and the broadband scores first, and then look at the results for each parameter. Fig. 17 shows S1 scores for each one of the ten parameters. The best results are for the duration, peak value parameters and response spectra (C1, C2, C5, C6, C7 and C8). The cross correlation, a parameter that is usually accepted to provide a meaningful measure of the misfit between signals, scores rather well, with the exception of USB. The scores of the integral parameters and Fourier spectra are more scattered. Regarding the integral parameters, this is to be expected because they accumulate the error and it becomes difficult to balance the discrepancies over time. Energy, though, seems to consistently give a slightly better

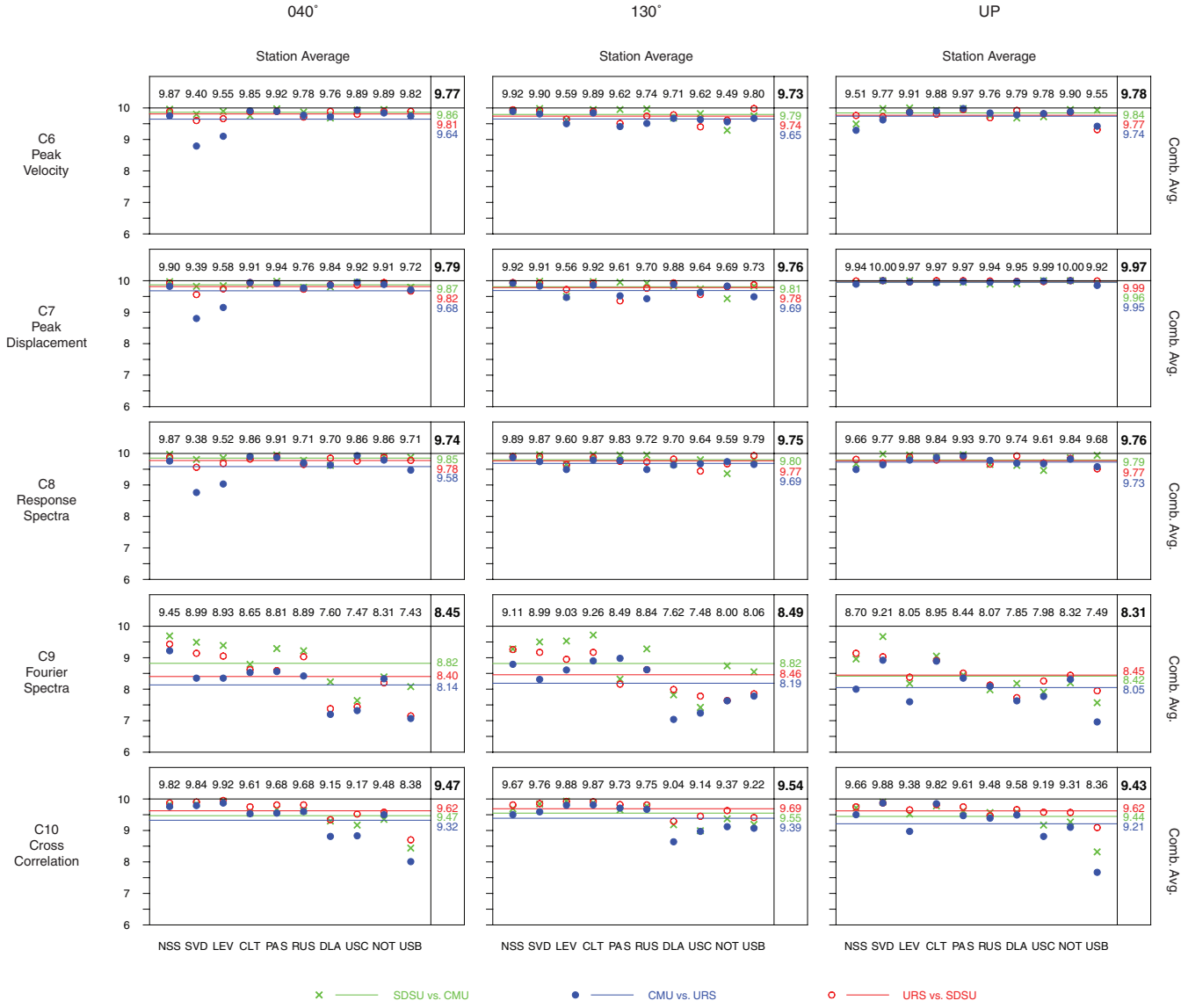

Figure 17. *(Continued).*

score than Arias intensity. We think this is because Arias intensity uses acceleration instead of velocity—the latter being smoother than the former, thus yielding better cumulative results. We also observe the Fourier metric to be quite sensitive to the highly oscillatory shape of the spectra—which is related to the number of samples used in the FFT. This may have brought down the scores. Despite the low scores, we chose not to apply any rule to smooth the spectra for the sake of transparency. After all, the scores for C9 are still good, and only those observation points in soft soil (DLA, USC), or the farthest from the fault (USB) have scores below 7.5—still within the range described by Anderson as a 'good fit' (i.e. from 6 to 8).

Despite the discrepancies mentioned above, we believe that the goodness-of-fit criterion and the different scores proposed by Anderson (2004) strengthen the preliminary conclusions we made based on the results of the misfit criteria. These metrics indicate that our simulations compare very well between each other and reinforce confidence in the results. This may be interpreted as an indication that for the engineering applications implicit in Anderson's metrics, there is no practical distinction between the corresponding individual simulations of the three groups. In the case of the goodness-of-fit we even got some scores very close to perfect. In the final global averages for all stations (see S1 top right-hand corner values at the bottom frames of Fig. 16), the three components of motion yield scores above 9.37. With the exception of the Fourier spectra, the global averages for the analysis of individual parameters (Fig. 17) are all above 9.07. While closer agreement has been achieved in horizontally stratified models or homogeneous models (e.g. Faccioli *et al.* 1997; Komatitsch & Tromp 1999; Käser & Dumbser 2006; Kristekova *et al.* 2006), to our knowledge, no verification has ever been done before for ground motion simulations in regional-scale realistic 3-D models. We find the present results to be quite encouraging, especially given the level of complexity involved in this kind of simulations. Nevertheless, we wonder what the sources of the discrepancies might be. We devote the next section to discuss these and other relevant insights about the accuracy of our simulations and validity of our results in light of the verification process.

7 DISCUSSION OF RESULTS

Even though the individual simulations are theoretically based on the same prescribed velocity and intrinsic attenuation models, and on the same earthquake source, there are some intrinsic differences between the methods and their implementations. We think that the discrepancies observed in the verifications above, though minor, are the result of these intrinsic differences. It is important to try to identify their cause. We have found that much of the discrepancies stem primarily from differences in the grids used in the two FDM codes, and between these grids and the unstructured mesh used in the FEM code. Other reasons for discrepancy are differences in how the intrinsic attenuation and the absorbing and traction-free boundary conditions are modelled in the three codes, and, to a lesser extent, differences in the processing of the input and output data.

We discuss these possible sources of discrepancies and the ensuing consequences based on the assumption that their resolution would eventually yield a perfect fit of all three simulation sets, but with the understanding that resolving these discrepancies implies, in most cases, expensive restructuring of the simulation codes. This is beyond the scope of this paper, as we do not necessarily consider it crucial to fully resolve all differences, given the excellent level of agreement reached already.

7.1 Resolution

We start by considering the one aspect we think most broadly affects the results: the difference between the two regular nodal-based grids used in the FDM codes, and between them and the element-based mesh used in the FEM code. As described in Section 5, both URS/USC and SDSU/SDSC groups use a staggered-grid FD technique, fourth order in space and second order in time, whereas CMU/PSC uses an octree-based FE mesh, second order in both space and time. In theory, and provided they use a sufficiently refined grid and mesh, both methods are expected to yield satisfactorily approximate results. Fig. 18 depicts the mesh and grids used by each group. Here, one can see the difference between the unstructured implementation by CMU/PSC—in which mesh-size is tailored to shear velocity wavelength—and the regular grids of 100 and 200 m for SDSU/SDSC and URS/USC, respectively. As mentioned before, URS/USC uses a smaller domain than the other two and a different coordinate transformation—something that will be discussed ahead. The fact that the SDSU/SDSC grid is twice as fine as the URS/USC grid suggests that the former should yield a higher degree of accuracy than the former. The extra-refined SDSU/SDSC grid was created for a 1-Hz simulation. Such refinement is unnecessary for the field-variable discretization, given present simulation requirements of $V_{s_{\min}} = 500\ \mathrm{m\,s^{-1}}$ and $f_{\max} = 0.5$ Hz, for which a grid size of 200 m provides five points per minimum wavelength of the shear waves, which, as discussed in Section 5, is regarded as suitable for the staggered-grid FD technique used by the SDSU/SDSC and the URS/USC codes. On the other hand, a more refined discretization of the material properties distribution improves accuracy. For example, the tailored CMU/PSC mesh includes refinements in the soft-soil regions with element size down to 73.2 m, corresponding to more than 13 points per wavelength. As expected, a higher density of the nodal distribution seems to lead to an increase in accuracy. This can be observed from the results in Fig. 12 at the RUS station, located on an alluvial soil, for which the agreement between amplitudes of the Fourier transforms of the SDSU/SDSC and CMU/PSC synthetics at the higher frequencies is closer than with respect to the URS/USC synthetics.

7.2 Coordinate transformation

Also noticeable in Fig. 18 is the 'curvature' in the URS/USC grid plot due to differences in the schemes used to transform latitude and longitude into local x, y coordinates. CMU/PSC and SDSU/SDSC use a bilinear interpolation based on the four corners of the domain, while URS/USC uses a spherical transformation based on the dimensions of the domain, its rotation with respect to north, and the location of the middle point of the domain at the surface. All three groups' domains are, in fact, rectangular prisms (or cuboids) in their own local coordinate systems, but when seen from another coordinate system, this difference surfaces. That is the case in Fig. 18, which is plotted using the coordinate system of CMU/PSC and SDSU/SDSC. We believe that since each group is self-consistent when feeding the model or extracting data from it, no major discrepancy should result from this 'curvature' issue. It, however, implies that, depending on the model used as reference, waves travelling from one end of the domain to the other, will be seen as doing so along a curved line rather than a straight one in a different model. That curvature, however, is of only a fraction of a degree ($<0.48^{\circ}$). We believe discrepancies attributable to this effect to be negligible, as manifested by the matching *P*-wave arrival times in Figs 10 and 11.

7.3 Actual models and material properties

The three modelling groups use the same CVM-Etree as their common material model to query the properties to be used in their actual simulation models. However, because they have different nodal distributions as well as different number of points per wavelength, p, as illustrated in Figs 19 and 20, they actually query and retrieve information from the CVM-Etree at different locations and use this information differently in the construction of their respective

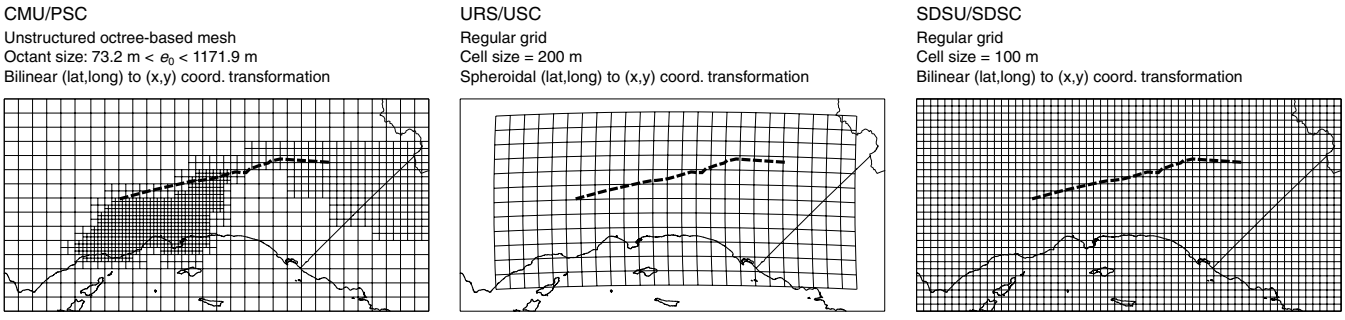

Figure 18. Depiction of the plan view at the free surface of the regular grids built for the two FDM codes and the octree-mesh generated by the FEM code, plotted in the x, y local coordinate system used by CMU/PSC and SDSU/SDSC. The mesh and grids shown here are just a representation of the actual ones.

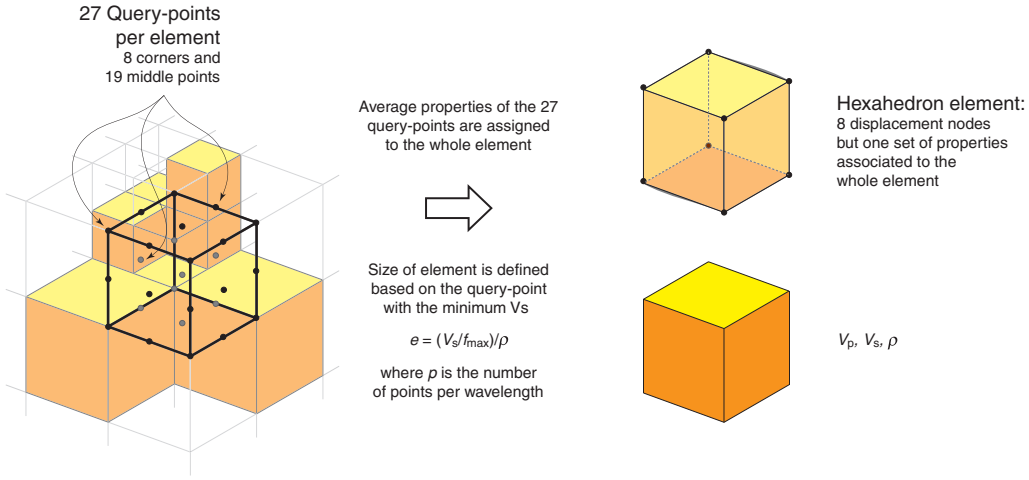

(a) CMU/PSC's octree-based finite element mesh

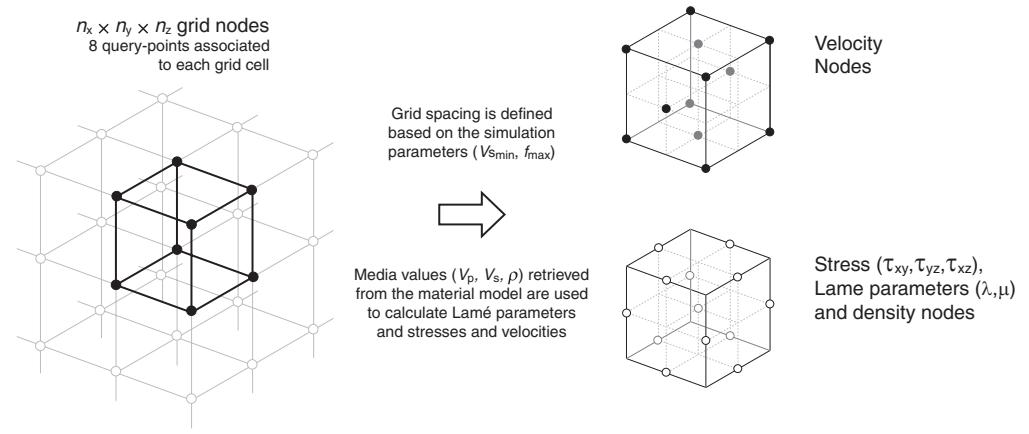

(b) SDSU/SDSC and URS/USC's finite differences staggered-grid

Figure 19. Schematic description of the procedure of querying the material model properties and assigning them to the actual models in the simulation for (a) the FEM and (b) FDM implementations.

simulation models. This may be, perhaps, the main cause for the discrepancies between the various results. The CMU/PSC code assigns properties to elements rather than nodes. During meshing, a recursively adaptive procedure defines the element size based on the minimum V_s value of 27 query-points in the cube that defines an octant-element (Fig. 19a). Each element's set of properties (V_p, V_s, ρ) is then assigned as the corresponding average of these 27 query points. In contrast, in the FDM codes, values are extracted from the CVM-Etree for a predefined fixed regular grid of nodes ($n_x \times n_y \times n_z$), which are later manipulated to obtain the media parameters that will be used in the cell-nodes of the staggered-grid formulation (Olsen 1994; Graves 1996a). The cell nodes, however, are not necessarily collocated on the same grid nodes (see Fig. 19b); neither are their properties directly assigned as extracted from the CVM-Etree. That is because in the staggered-grid FDM approach, the properties are averaged arithmetically or harmonically (see Section 5) based on neighbouring cell-nodes to set their stress, Lamé and density values depending on the node's type (Fig. 19). The effect of this mismatch between nodes, cells and elements, is that properties from the material model are neither extracted from the material model, nor assigned to the simulation models, at the exact same locations. Even if they were, since the averaging procedures are different, they would end up not being identical in any case.

For homogeneous and quasi-homogeneous regions, or regions with gradual changes in properties, this situation is not a problem, but for highly heterogeneous and rapidly changing formations, as is the case here, this causes the actual simulation models to have different material structures. Fig. 20(a) shows slices of the actual models for V_s at the free-surface. Fig. 20(b) shows the difference of each slice of V_s values with respect to the others. We detect minor (<200 m s^{-1}) and moderate (<500 m s^{-1}) differences spread in the central basins, and greater discrepancies (>500 m s^{-1}) concentrated along the border that defines the Salton Trough region. This is due to the difference in grid size sampling locations and treatment of the retrieved material properties between the various computational models.

This comparison implies that in the central region the SDSU/SDSC model is slightly stiffer than the URS/USC model, and the CMU/PSC is slightly softer than the other two, whereas on the border of the Salton Trough area, the CMU/PSC model is stiffer than the SDSU/SDSC one, and the latter stiffer than URS/USC. This, however, is only at the free surface. We know that these relations do not necessarily hold at depth because properties for the

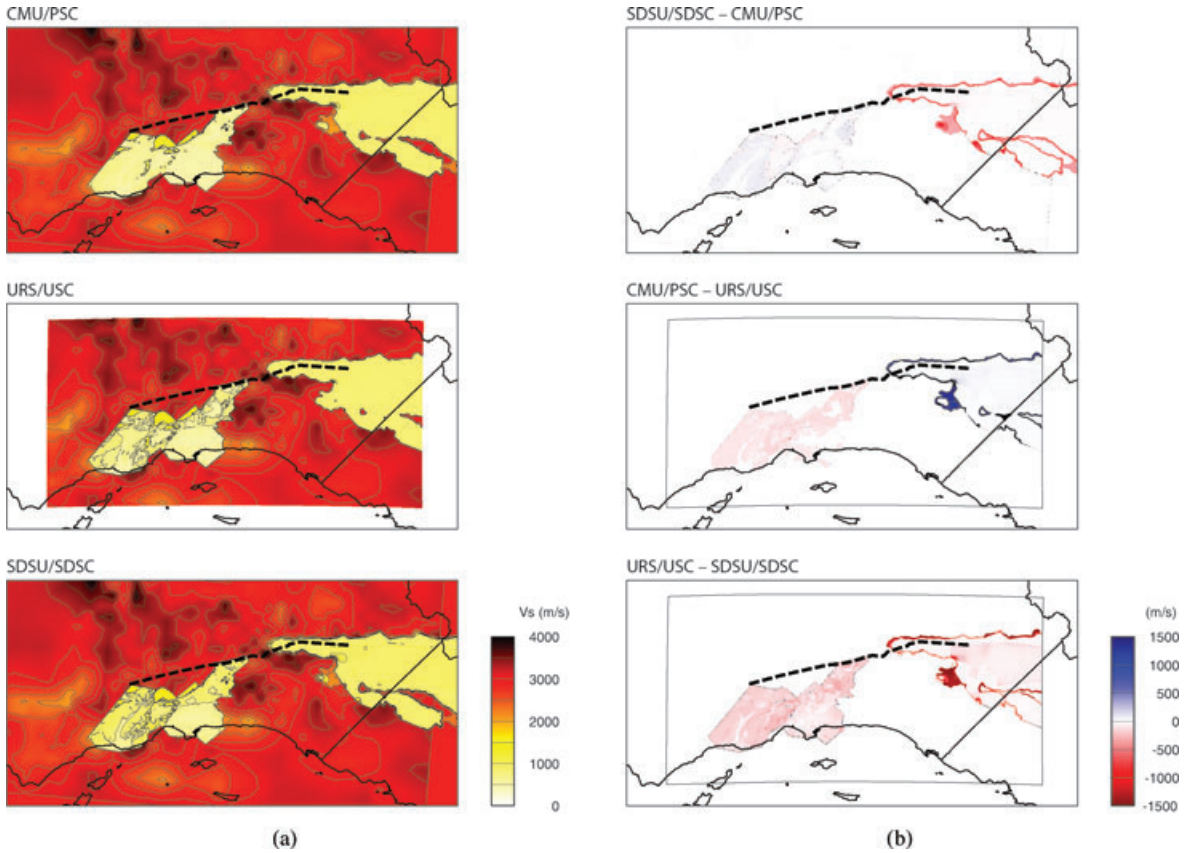

Figure 20. Comparison between the different discretized versions of the material models at the free surface built by the three groups based on the CVM-Etree for (a) the values of V_s and (b) the differences between each other.

different models 'change' with depth at different spatial rates—from their different resolutions and assignment rules. Therefore, truly identifying which model is stiffer or softer would require a similar comparison at different depths. Our experience is that, in the basins, the two FDM models end up being generally softer than CMU/PSC model—SDSU/SDSC being the softest of the three. This is supported by the results, which generally yield larger peak velocity and energy values for SDSU/SDSC (see Figs 10 and 11).

Consequences of discrepancies in the actual material models are: (i) faster or slower surface waves within the basins and away from the fault as noted from the phases—this appears to be the case at observation points like DLA, USC, NOT, and USB and (ii) differences in the envelope of synthetics, in magnitude and shape—especially noticeable during the 50 s following first arrival of waves at stations like DLA and USB. Since the sampling differences affect primarily frequencies higher than the maximum frequency of interest (0.5 Hz) in the present verification exercise, and because the exact sampling depths and rate were in each case designed to capture approximately the local wavelengths, we believe these discrepancies to be minor—nonetheless, present. Additionally, we know these differences vanish with depth as the model gradients become less steep.

It should not go without mentioning that, though the Southern California model exhibits several sharp interfaces as shown in Figs 5 and 21, other basins around the world exhibit higher contrasts between the softer sediments and the underlying bedrocks. The Valley of Mexico represents an extreme example. Additional care would be required both in meshing and in the material grid parametrization of such situations.

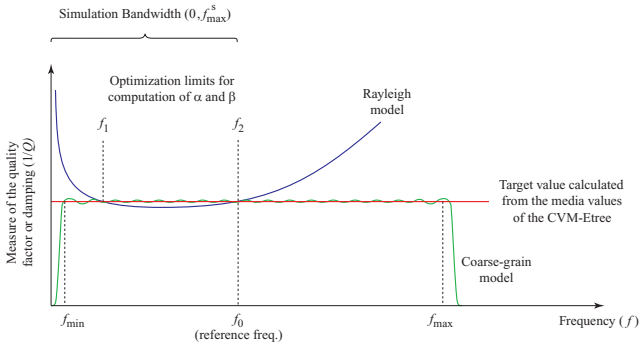

Figure 21. Schematic representation of the two approaches to intrinsic attenuation implemented in the simulation codes.

7.4 Non-planar source implementation

As mentioned in Section 3, the source that defines the ShakeOut earthquake scenario was designed by an interdisciplinary group led by the USGS (Jones *et al.* 2008). This group first defined a static slip description of the fault, then computed a planar kinematic rupture, and finally mapped the kinematic source onto an adjusted version of the non-planar fault geometry defined in SCEC's CFM—a triangular-elements 3-D-representation of California's faults geometry. The source was then provided to the simulation groups in the form of a collection of point sources that, as a set, define the complete rupture. As expected, the location of the point sources in the collection do not match exactly the geometry of the FDM grids, nor that of the FEM mesh. As a result, each group had to translate

the characteristics of each point source into a convenient format. In the case of the FEM code, CMU/PSC converted each point source (double couple) that falls within a given element, into equivalent forces at the eight corner nodes of the element that includes the point source. In the case of the FDM codes, this is done by inserting a moment rate source as an extra component to the stress tensor of each cell.

In principle, all three approaches are equivalent. For a single point source and for an embedded extended source in a layered medium, differences in ground motion at the free surface (away from the source) are small (Day *et al.* 2001, 2003). The similarity of the results in Figs 10–12 suggests that this is true also for the more complex ShakeOut scenario. There is, however, the fact that both approaches try to represent a dislocation by approximating it as a sudden change in the continuum. As stated, this should have no effect away from the source, where the numerical approximation moves closer to the exact solution as one moves away from the fault. However, very near to the fault, the differences in grid and mesh resolutions may become a key factor and thus a possible explanation for the minor discrepancies observed at stations NSS, SVD and LEV (Figs 10 and 12).

7.5 Attenuation

As we saw in Section 5, both for URS/USC and SDSU/SDSC, the anelastic attenuation was modelled using the relations $Q_s = 50V_s$ and $Q_p = 2Q_s$(V_s given in km s^{-1}), whereas CMU/PSC uses a general value of $Q = 50V_s$ that does not explicitly distinguish between *P* and *S* waves.

The URS/USC and SDSU/SDSC implementations consist of the coarse-grained representation of a discrete relaxation spectrum approximating frequency-independent Q, introduced by Day & Bradley (2001); in the case of URS/USC, further refinement was adopted following the improvements for low values of Q proposed by Graves & Day (2003). In this scheme, the model is characterized by a logarithmic attenuation function $1/Q(\omega)$, where ω is the frequency in radians per second. This function is assumed to be known within a bandwidth of interest ($\omega_{\min}, \omega_{\max}$). The lower and upper cut-off frequencies, $\omega_{\min}$ and $\omega_{\max}$, are set such that attenuation below and above them can be ignored. The choice of these limits is guided by the desire to have Q effectively constant over some bandwidth that includes the simulation bandwidth. The attenuation model renders the elastic moduli (and therefore the wave speeds) frequency dependent, with unrelaxed (i.e. infinite frequency) limiting values appearing explicitly in the FDM solvers. This physical dispersion raises the issue of how these frequency-dependent quantities are related to the velocities extracted from the CVM-Etree. We assume that the CVM wave speeds are to be interpreted as phase velocities at a reference frequency ω_0 lying within the target bandwidth of the simulations. A second issue is then how the unrelaxed moduli are calculated from the reference-frequency values. SDSU/SDSC calculates the unrelaxed moduli from the reference-frequency values using expressions given by Day & Bradley (2001), while URS/USC uses a more elaborate procedure based on Graves & Day (2003) that is equivalent to the SDSU/SDSC procedure for moderate values of Q, but more accurate for very low Q. Each procedure takes into account the upper absorption-band limit $\omega_{\max}$. The differences between these two implementations should be negligible for values of Q larger than the lowest Q of 25 (for $V_{s_{\min}} = 0.54$ km s^{-1}) used in this study, provided both codes use the same reference frequency, and provided the upper absorption-limit frequencies used (even if they are different from each other) are both well above the upper bandwidth target of the simulations. Both URS/USC and SDSU/SDSC used the following values for the limit and reference frequencies (in Hz): $f_{\min} = 0.01$ Hz, $f_{\max} = 25.0$ Hz and $f_0 = 0.5$ Hz. Traditionally, a value of $f_0 = 1$ Hz has been used in many seismological applications (Aki & Richards 1980). It seems natural to take some frequency within the seismic band as the reference frequency, since that is where the velocity model has actually been determined. Here, we have selected f_0 to be the upper valid limit of the simulation, implying that the frequencies below that value will have velocities slightly slower than those extracted from the CVM-Etree. On the other hand, the selection of $f_{\min}$ and $f_{\max}$ is based on our desire to have a Q that is effectively constant over a broader bandwidth than the desired for our simulation, while keeping $f_{\min} < f_0 < f_{\max}$, and satisfying other practical considerations regarding the finite dimensions of the grid and the time-step of the simulation (see Day & Bradley 2001).

The CMU/PSC implementation uses Rayleigh damping, a form of viscous damping, in which the discretized element viscous damping matrix is expressed as a weighted sum of the mass and stiffness matrices; that is, $\mathbf{C} = \alpha\mathbf{M} + \beta\mathbf{K}$, where $\mathbf{M}$ and $\mathbf{K}$ are the mass and stiffness matrices of each element, and α and β are coefficients determined from $1/Q(\omega) = \alpha/\omega + \beta\omega$ using least squares over a selected bandwidth (ω_1, ω_2), in order to minimize the difference of $1/Q(\omega)$ with respect to the constant target value $1/Q = (50V_s)^{-1}$ (Bielak *et al.* 1999). This approach has been successfully used in the past in similar applications (e.g. Bielak *et al.* 1999). Because $1/Q(\omega)$ behaves as $1/\omega$ for small frequencies and as ω for large ones, we have found that this model works well for small bandwidths (e.g. $f \leq 1$ Hz) and small values of α and β ($\ll 1$), like the ones considered here, though it will need to be modified for future cases with wider bandwidths of interest. For the present simulation, $f_1 = 0.2\ f^s_{\max} = 0.1$ Hz and $f_2 = f^s_{\max} = 0.5$ Hz, where $f^s_{\max}$ is the simulation upper frequency limit. In Rayleigh's damping there is no concept of a maximum frequency as understood in the coarse-grained approach, and there is no recentring of the material values. The method assumes that the media values extracted from the CVM-Etree correspond to the case without attenuation. The variability of the moduli with frequency is adjusted implicitly by the introduction of the viscous damping term $\mathbf{C}\dot{u}$ into the FE semi-discretized equations of motion, where $\dot{u}$ is the nodal velocity.

The behaviour of $1/Q$ with frequency for the two attenuation models adopted by the simulation groups is depicted in Fig. 21. We see how the approach adopted by the FDM codes adjusts the unrelaxed modulus such that the frequency-dependent modulus conforms to the CVM-Etree target at the reference frequency and over a wide range of frequencies around it. The approach in the FEM code is to minimize the error around the target value within a prescribed frequency band. Given that the simulation is aimed to be valid within a limited bandwidth, the discrepancies between these two approaches are expected to occur mainly at the lower portion of such band ($f < f_1$). Since the energy of the ground motion is concentrated above that threshold ($f > f_1 = 0.1$ Hz), as can be seen from the spectra in Fig. 12, we do not expect this to be a major factor in the discrepancies. Both intrinsic attenuation models are introduced to represent the dispersion of the prescribed physics. Because of their different nature, the relevant issue is to determine the relative dispersion between the different attenuation models. Our simulations suggest that the physical dispersion is negligible within the bandwidth of interest. This can be seen by comparing the anelastic results with those for the purely elastic case. Fig. 22 shows such comparisons at station DLA (130° component) for each

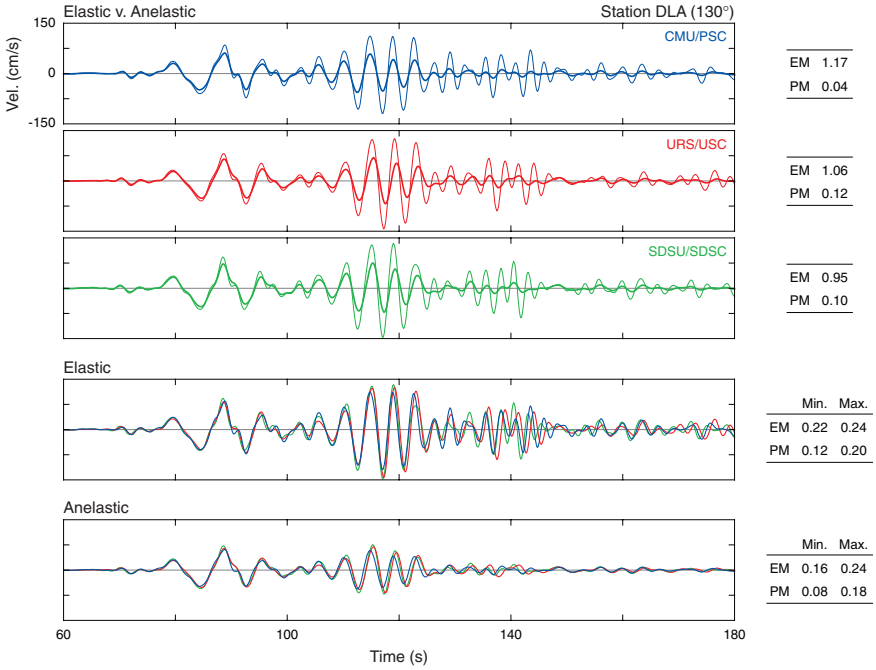

Figure 22. Individual comparison of anelastic (thick line) and purely elastic (thin line) results for the three simulation groups at station DLA, component 130°, and comparisons between the groups for the two cases: with and without attenuation. Misfit single-value scores to evaluate each comparison are shown on the right-hand side.

simulation group. At this location, the effects of attenuation are quite significant on the amplitude of the ground motion with either attenuation model. Yet, we observe little to almost no dispersion. This can be seen by comparing the values of the phase misfit shown in the top three panels between the elastic and anelastic synthetics from each group with the corresponding values of *PM* across simulations, shown separately for the elastic and anelastic cases in the bottom two panels. We first observe that the differences in *PM* between the different simulations of the anelastic case are somewhat smaller than for the elastic problem. This suggests that for our test case the intrinsic attenuation does not introduce an additional numerical error over that of the purely elastic model. In addition, the values of PM between the elastic and anelastic simulations shown in the top three panels are generally smaller than the corresponding values in the bottom two. This, in turn, suggests that the discrepancy in phase due to the physical dispersion is smaller than the numerical dispersion observed between the simulations from the three different groups.

Fig. 22 also compares the three groups' purely elastic synthetics for the same station all together. It is noteworthy from the two lower panels that the differences between the individual elastic synthetics, both in amplitude and phase, are of the same order, or even greater than the corresponding differences for the anelastic simulation—as inferred from the *EM* and *PM* minimum and maximum values obtained for the different combinations and shown to the right of the panels. This strengthens the indication that the observed differences between the individual simulations are due primarily to numerical integration of the governing equations of motion and discretization of the material model, and not to the different anelastic models. As a confirmation, we also tested cases with the two FDM codes with different reference frequencies and found that a difference of a factor of 2 in f_0 would yield a relative dispersion of only 0.2 per cent, albeit with larger differences in amplitudes. Lastly, observe that the effect of anelastic attenuation is most prominent for the surface waves (∼110–130 s). The difference in the maximum amplitude between the elastic and anelastic waves is on the order of 100 per cent. This corresponds to values of $EM > 1$. This and other differences between the elastic and anelastic results are of interest to ongoing studies dedicated to the analysis of the physics of this and similar simulations in the region.

7.6 Boundary conditions

7.6.1 Free-surface

The numerical solution of the discretized equations of anelastic wave propagation must satisfy a traction-free boundary condition on the free surface. This condition is satisfied naturally in the FEM; convergence to the exact zero-traction with decreasing mesh size is of the same order as for stresses within the domain. In the FDM, however, the traction-free condition needs to be imposed explicitly. The codes that use the velocity–stress staggered-grid FDM formulation have adopted an explicit formulation that requires two (virtual) grid planes above the free surface, half grid point apart vertically, and thus offers two different possibilities for its implementation (Levander 1988; Graves 1996a). The first plane is collocated at the normal stress positions, and the second one is at the *xy* and *yz* stresses. Following the Gottschammer & Olsen (2001) notation, they are, respectively, called FS1 and FS2. URS/USC uses the FS1 implementation and SDSU/SDSC uses FS2. While both formulations have proven to be accurate, differences between them and with respect to the exact solution are possible. Moreover, in recent years other more accurate representations of the traction-free boundary conditions have been developed (Kristek *et al.* 2002; Moczo *et al.* 2007). Here we limit ourselves to the methods we have implemented and used.

Motivated by a preliminary test in which they found that synthetics computed using the two different boundary conditions showed

some differences, Gottschammer & Olsen (2001) investigated the misfit between FS1 and FS2 with respect to the exact solution of a point source in a uniform half-space. They found FS1 to be more accurate for the horizontal components of motion, whereas FS2 to yield smaller misfits for the vertical component. They also found FS2 to be generally more accurate than FS1 near the epicentre. The misfits found by Gottschammer & Olsen (2001) between FS1 and FS2 for the homogeneous half-space are of the order of 10 per cent, similar to those we observe in our comparisons.

7.6.2 Absorbing Boundaries

Each simulation group used different absorbing boundary conditions to limit the spurious reflections at the truncation boundaries. CMU/PSC used a plane-wave approximation represented by viscous dampers for *P* and *S* waves (Lysmer & Kuhlemeyer 1969). Similar treatment is followed by URS/USC, where a parabolic plane-wave approximation associated with a simple *P*- and *S*-wave decomposition for the particle-velocity components is considered, after Clayton & Engquist (1977). In contrast, SDSU/SDSC uses a more accurate implementation based on the multi-axial perfectly matching layers (M-PML) adapted from the original formulation in electromagnetism by Berenger (1994) and its implementation in a staggered grid by Marcinkovich & Olsen (2003).

While the reflected waves are generally small compared to the outgoing waves, a careful analysis of snapshots of the wavefields and synthetic seismograms reveals their presence late in the simulations. These spurious reflections only affect areas near the edges of the simulation domains. The clearest cases of artefacts from the boundaries are found near the NW (left-hand) boundary, enhanced by rupture directivity and wave guide effects for the northwestward rupture propagation. This is illustrated in Fig. 8, where such artefacts occur at 150 s for the smaller simulation domain of URS/USC and at 180 s for the larger domains of CMU/PSC and SDSU/SDSC. These artefacts are on the order of only 2 per cent of the PGV and while present, they are a minor source of error. In particular, they do not affect the envelope and phase misfits between the different groups synthetics presented in our study.

7.7 Data extraction

Table 2 summarizes the selection of parameters made by each group to output the results. For the free surface wavefield—used for presenting regional results, for example, Figs 8 and 9—each group recorded the ground motion on a regular grid, at a larger Δt than that required for the simulation, that is, every n simulation time-steps. Two of the groups used the same output Δt as the simulation Δt for the selected locations used for comparison. As shown in the table, all three groups used a different spatial resolution. Discrepancies caused by the different spatial resolutions or mismatching time step are visible only at high definition plots and are typically of minor importance. These parameters, however, do more evidently affect the comparison of synthetics at selected locations. Both URS/USC and SDSU/SDSC extract the signals at the nearest point of their respective regular grid. This introduces an error that depends on the distance from the station to the nearest gridpoint. On the other hand, the CMU/PSC scheme interpolates at run-time within the FE that contains the point of interest. In either case, the worst scenario would be when the point of interest is in the middle of a cell or element. When one compares all possible cell corners graphically, there is no visible difference, but if one runs a check using the misfit criteria, discrepancies will surface. We tested the case of a station (USC) in soft soil (i.e. high spatial variability) and found that the maximum values for *EM* and *PM*, in a cell of 200 m, would be of the order of 0.06. If we compare this value to the global averages shown in Fig. 15, it will reaffirm the notion that the existence of an original misfit carried on from the differences in the implementations makes the phase discrepancies almost negligible, and the envelope misfit less significant.

Table 2. Summary of output parameters.

	CMU/PSC	URS/USC	SDSU/SDSC
Free-surface grid			
Field	Displacement	Velocity	Velocity
Resolution	1000 m	600 m	500 m
Output Δt	0.10 s	0.20 s	0.11 s
Selected locations			
Field	Displacement	Velocity	Velocity
Resolution	Variable	200 m	100 m
Location	Interpolation	Nearest point	Nearest point
Output Δt	0.01 s	0.01 s	0.11 s
Simulation Δt	0.01 s	0.01 s	0.0055 s

Notes: In the upper half, resolution refers to a regular grid of nodes used for the free surface snapshots, while in the lower half, resolution refers to that of the internal FDM grids or FEM mesh implementations used to record ground motion at select locations.

7.8 Data manipulation

Last but not least, is the manipulation of data during the pre- and post-processing phases. In the pre-processing phase of earthquake simulations, we use two major input sets of data: (i) the source description and (ii) the material model. We have already shown how both get affected by each independent implementation based on the difference between the grids and mesh. In addition, in the pre-processing phase, the collection of slip-rate functions that define the source are low-pass filtered and resampled by each group at their convenience, to satisfy the simulation parameters and numerical requirements, and to acquire information from their respective models. During the post-processing phase, in order to apply the verification metrics discussed in Section 6.2, we needed to have all synthetics with a common Δt and frequency bandwidth. Thus, we bandpass filtered and resampled the results again. The bandpass filtering was done using a zero-phase trapezoidal Ormsby filter with two ramps, one high-pass ramp at the zero end and a low-pass ramp at the $f_{\max}$ end. Besides having a common bandwidth, the high-pass filter was applied to eliminate numerical errors from the integration of synthetics needed for comparisons with the goodness-of-fit criterion, and the low-pass filter was applied to avoid aliasing problems during resampling. Table 3 summarizes the filtering and resampling characteristics each group used in pre-processing the source and those that were used for all output sets during post-processing.

In the pre-processing phase, each group used different filter parameters and resampled the source description to its respective simulation time-step. Both CMU/PSC and URS/USC used zero-phase filters. That was not the case of SDSU/SDSC where a delay of ∼7.5 s was introduced. This delay was then corrected in the post-processing phase. Both CMU/PSC and SDSU/SDSC used larger values for their filters' corner frequencies because their meshes were designed to capture waves of frequencies higher than the 0.5 Hz limit imposed for the current simulation, while URS/USC kept the cut-off frequency at such limit. In order to examine the effect that these cut-off frequencies had on the actual source within

Table 3. Summary of filtering parameters applied in the pre-processing phase on the slip time-functions of the source description, and in the post-processing phase on the synthetics subjected to the verification metrics.

	Slip time-function (pre-processing)			Synthetics (post-processing)
Group	CMU/PSC	URS/USC	SDSU/SDSC	All
Filter	Butterworth	Butterworth	Butterworth	Ormsby
Domain	In frequency	In time	In time	In frequency
Passes	–	1 fwd., 1 rev.	2 fwd.	–
Order/Poles	14	4th	4th	–
Phase shift	–	–	− 7.5 s	+7.5 s
Corner freq.	1.8 Hz	0.5 Hz	1.0 Hz	–
High-pass ramp	–	–	–	0–0.05 Hz.
Low-pass ramp	–	–	–	0.475–0.525 Hz.
Resampling at[a]	0.01 s	0.01 s	0.0055	0.1 s

[a]Original Δt was 0.1 s.

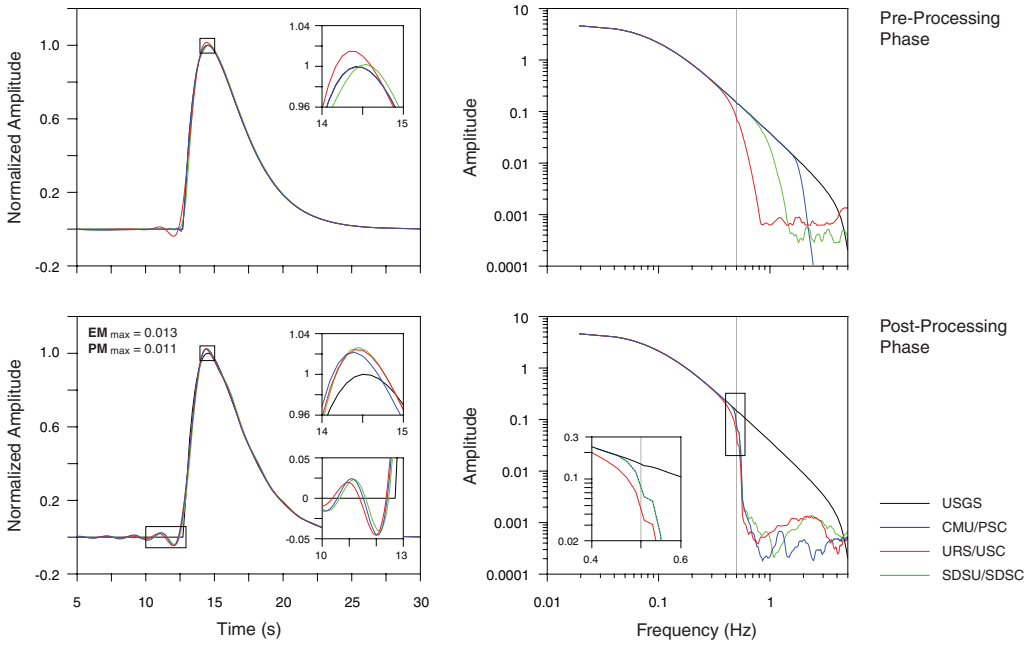

Figure 23. Effects of pre- and post-processing filtering of input and output. The top row shows the effect on a randomly selected slip-rate function from the originals provided by USGS. The bottom row shows the final effect of pre and post-processing applied to synthetics as if it were applied to the source function. The vertical grey line in the spectra shows the upper frequency limit of the simulation, $f_{\max} = 0.5$ Hz. The bottom left-hand panel includes the maximum values of *EM* and *PM* obtained from comparing the three groups final slip-rate functions.

their respective models, Fig. 23 (top panel) shows the slip-rate function of a point source (randomly selected from the collection defining the rupture), and the results of each group filter applied to it. Slight differences may be seen in the (peak) amplitudes and phases (of the initial jump). In this figure, and for all post-processing, we have shifted back (or recentred) SDSU/SDSC source function and synthetics so that we can focus in the actual discrepancies. Differences in the peak amplitudes are of the order of 1–2 per cent and in phases of about 1/2 to $1\Delta t$.

Considering that the simulation rupture consists of about 50 000–100 000 point sources for the individual groups, we think that this difference, though small for an individual source, may have accumulated over the entire rupture and contributed to the larger differences observed in the results. More important to our verification effort then, is to investigate the final effect in the synthetics used for the comparisons. Since our synthetics are not identical, it is difficult to isolate the effect of the filtering processes alone. We can, however, do it indirectly by applying the same filters we used in pre- and post-processing, to the input functions. Because the system is linear, the sum of the two filters applied to each set would have the same effect on the results as if we applied them to the input.

Fig. 23 (bottom panel) shows the total effect of pre- and post-processing low-pass filtering applied to the same slip-rate function as an alternative to understanding the overall effect on the synthetics. (We have not included the high-pass filter used during post-processing because it has a common effect on all groups' synthetics and, as mentioned above, it was done only for signal-processing purposes, thus has no effects in the comparisons—as seen from Fig. 12.) Fig. 23 shows that, after low-pass filtering in the post-processing phase, the difference between the groups' peaks is reduced to about 1 per cent, the difference in the phases remains on the order of 1/2 to $1\Delta t$. In terms of the misfit criteria, the corresponding single-value scores for this comparison are $EM_{\max} = 0.013$ and $PM_{\max} = 0.011$. This confirms our observations on the input. It also relates to the

synthetics compared in Fig. 10, and the results presented in Fig. 14, in that the final *EM* and *PM* scores carry an original misfit from the input, which is about 8 per cent and 12 per cent of the final average values presented in Fig. 15 ($EM_{\max} = 0.17$ and $PM_{\max} = 0.09$).

We have also compared the effect of filtering in the frequency domain and found that having applied the same filter in the post-processing phase is favourable to the comparison between CMU/PSC and SDSU/SDSC—which fall one on top of the other—but affects the results of URS/USC because the filter applied during pre-processing by URS/USC also had a corner frequency of 0.5 Hz (which is the central frequency of the ramp of the filter applied during post-processing). This double filtering at 0.5 Hz may be one reason for the URS/USC synthetics to systematically show a lower content of energy in the highest frequencies of the bandwidth (Fig. 12).

8 CONCLUDING REMARKS

We have presented the verification of results for the ShakeOut earthquake scenario obtained by three different simulation groups. One group used a FE approach and the other two staggered-grid FDs. We reviewed the concept of verification in the context of numerical simulations, applied it to earthquake simulations, and proposed an adaptation of the verification and validation paradigm. We reviewed the concepts of graphical verification and discussed why this type of verification for simulations of this kind, although appropriate as a first qualitative assessment, is insufficient for accurately estimating the level of agreement between two or more sets of results. To overcome this situation we employed two different methods (Anderson 2004; Kristekova *et al.* 2006) as a means to do a thorough verification of the results and implementations of the three simulation groups. Our results yield small misfit values according to the different criteria proposed by Kristekova *et al.* (2006). On average, we observed an envelope misfit of 0.17 over 10 representative observation points for the three components of motion, and a misfit of 0.09 for the phases. On the other hand, according to the procedure proposed by Anderson (2004), we obtained an overall average goodness-of-fit score of 9.37. This suggests that the agreement between the three sets may be regarded as remarkably good.

Despite these positive results, we investigated the possible causes of discrepancies and found that, although, in principle, we targeted the same problem using the same input data, some differences lay beneath the details of each group's implementation. Most of these differences were identified to be intrinsic to the methods—derived from the fact that the FE approach uses an element-based mesh while the FD approach uses a nodal-based grid structure, which have different resolutions and orders of convergence. This, in addition to the differences between the groups regarding the simulation domain geometric characteristics, resulted in dissimilar discrete representations of the material structure and different translations of the source description into the computational models used by each group, and caused noticeable differences in the velocity contrasts at the material interfaces of the structural computational models.

Although we believe that these are the major causes for differences between the three sets, we performed a comprehensive analysis, seeking to examine the way each group interprets, operates and manipulates the data. We examined how each group imposes absorbing and free-surface boundary conditions, as well as their implementation of intrinsic attenuation or damping. We also found that there are minor details related to filtering and extraction of data that may be additional causes of discrepancies. In particular, we observed that the different attenuation models and the pre- and post-processing of data, as well as the different approaches to the extraction of synthetics at particular locations, all carry on an intrinsic or original misfit that may account for up to 30 and 70 per cent of the final envelope and phase misfits, respectively. This leaves the difference between the mesh and grids structures, and its consequences for material model discretization, as the major source of discrepancies. Differences in the methods used to impose interface traction continuity conditions, and thus material contrasts, may also have played a role.

Based on the results of this verification, we conclude that in light of the complexity and size of the problem, and considering we use different methods and implementations, our results are in very close agreement, and our codes are sufficiently robust and reliable to conduct independent or complementary studies of ground motion modelling in large regions. Clearly, new developments in FD and FE methodologies will be gradually incorporated into our codes in time. We expect that the agreement between the corresponding simulations will thus become even closer.

ACKNOWLEDGMENTS

This work was supported through NSF awards SCEC Petascale Cyberfacility for Physics-Based Seismic Hazard Analysis (PetaSHA-2) (EAR-0122464); SCEC Enabling Earthquake System Science Through Petascale Calculations (PetaShake) (NSF OCI-749313); Multiresolution High Fidelity Earthquake Modelling: Dynamic Rupture, Basin Response, Blind Deconvolution Seismic Inversion and Ultrascale Computing (NSF ITR/NGS-0326449) and Towards Petascale Simulation of Urban Earthquake Impacts (NSF OCI-0749227). SCEC is funded through the NSF Cooperative Agreement EAR-0106924 and USGS Cooperative Agreement 02HQAG0008. This research was supported by an allocation of advanced computing resources supported by the National Science Foundation. The computations were performed on BigBen at the Pittsburgh Supercomputing Center (PSC), DataStar at the San Diego Supercomputing Center (SDSC) and in part on Lonestar and Ranger at the Texas Advanced Computing Center (TACC). This research was also supported by an allocation through the TeraGrid Advanced Support Program. Computation for the work described in this paper was supported by the University of Southern California Center for High-Performance Computing and Communications. The SCEC contribution number for this paper is 1260. We thank Peter Moczo and an anonymous reviewer for their detailed reviews and constructive comments.

REFERENCES

Aagaard, B.T. *et al.,* 2008a. Ground-motion modeling of the 1906 San Francisco earthquake. Part II: ground-motion estimates for the 1906 earthquake and scenario events, *Bull. seism. Soc. Am.,* **98**(2), 1012–1046.

Aagaard, B.T. *et al.,* 2008b. Ground-motion modeling of the 1906 San Francisco earthquake. Part I: validation using the 1989 Loma Prieta earthquake, *Bull. seism. Soc. Am.,* **98**(2), 989–1011.

Adrion, W.R., Branstad, M.A. & Cherniavsky, J.C., 1982. Validation, verification, and testing of computer software, *Comput. Surv.,* **14**(2), 159–192.

Akcelik, V. *et al.,* 2003. High resolution forward and inverse earthquake modeling on terasacale computers, in *Proceedings of the 2003 ACM/IEEE Conference for High Performance Computing and Networking,* p. 8, IEEE Computer Society, Phoenix, Arizona.

Aki, K. & Richards, P.G., 1980. *Quantitative Seismology: Theory and Methods,* W.H. Freeman & Company, New York, NY.

Alterman, Z. & Karal, F.C., 1968. Propagation of elastic waves in layered media by finite difference methods, *Bull. seism. Soc. Am.,* **58**(1), 367–398.

Anderson, J.G., 2004. Quantitative measure of the goodness-of-fit of synthetic seismograms, in *Proceedings of the 13th World Conference on Earthquake Engineering,* International Association for Earthquake Engineering, Vancouver, BC, Canada, Paper 243.

Archuleta, R.J. & Day, S.M., 1980. Dynamic rupture in a layered medium: the 1966 Parkfield earthquake, *Bull. seism. Soc. Am.,* **70**(3), 671–689.

Archuleta, R.J. & Frazier, G.A., 1978. Three-dimensional numerical simulations of dynamic faulting in a half-space, *Bull. seism. Soc. Am.,* **68**(3), 541–572.

Balci, O., 1994. Validation, verification, and testing techniques throughout the life cycle of a simulation study, *Ann. Operat. Res.,* **53**(1), 121–173.

Bao, H., Bielak, J., Ghattas, O., Kallivokas, L.F., O'Hallaron, D.R., Shewchuk, J.R. & Xu, J., 1996. Earthquake ground motion modeling on parallel computers, in *Proceedings of the 1996 ACM/IEEE Conference on High Performance Networking and Computing*, p. 13, IEEE Computer Society, Pittsburgh, Pennsylvania, United States.

Bao, H., Bielak, J., Ghattas, O., Kallivokas, L.F., O'Hallaron, D.R., Shewchuk, J.R. & Xu, J., 1998. Large-scale simulation of elastic wave propagation in heterogeneous media on parallel computers, *Comput. Methods Appl. Mech. Eng.,* **152**(1-2), 85–102.

Berenger, J.-P., 1994. A perfectly matched layer for the absorption of electromagnetic waves, *J. Comput. Phys.,* **114**(2), 185–200.

Bielak, J., MacCamy, R.C., McGhee, D.S. & Barry, A., 1991. Unified symmetric BEM-FEM for site effects on ground motion—SH waves, *J. Eng. Mech., ASCE,* **117**(10), 2265–2285.

Bielak, J., Xu, J. & Ghattas, O., 1999. Earthquake ground motion and structural response in alluvial valleys, *J. Geotech. Geoenviron. Eng., ASCE,* **125**(5), 413–423.

Bielak, J., Ghattas, O. & Kim, E.J., 2005. Parallel octree-based finite element method for large-scale earthquake ground motion simulation, *Comput. Model. Eng. Sci.,* **10**(2), 99–112.

Boore, D.M., 1970. Love waves in nonuniform wave guides: finite difference calculations, *J. geophys. Res.,* **75**(8), 1512–1527.

Boore, D.M., 1972. Finite difference methods for seismic wave propagation in heterogeneous materials, in *Methods in Computational Physics,* Vol. 2, pp. 1–37, eds Alder, B., Fernbach, S. & Rotenberg, M., Academic Press, New York, NY.

Bouchon, M. & Aki, K., 1980. Simulation of long-period, near-field motion for the great California earthquake of 1857, *Bull. seism. Soc. Am.,* **70**(5), 1669–1682.

Bouchon, M. & Barker, J.S., 1996. Seismic response of a hill: the example of Tarzana, California, *Bull. seism. Soc. Am.,* **86**(1A), 66–72.

Brocher, T.M., 2005. Compressional and shear wave velocity versus depth in the San Francisco bay area, California: rules for USGS bay area velocity model 05.0.0, Tech. Rep. OFR-2005-1317, U.S. Geological Survey, http://www.sf06simulation.org/geology/.

Clayton, R. & Engquist, B., 1977. Absorbing boundary conditions for acoustic and elastic wave equations, *Bull. seism. Soc. Am.,* **67**(6), 1529–1540.

Day, S.M. & Bradley, C.R., 2001. Memory-efficient simulation of anelastic wave propagation, *Bull. seism. Soc. Am.,* **91**(3), 520–531.

Day, S.M., Bielak, J., Dreger, D., Larsen, S., Graves, R., Pitarka, A. & Olsen, K.B., 2001. Test of 3D elastodynamic codes, Tech. Rep. 1, Pacific Earthquake Engineering Research Center.

Day, S.M., Bielak, J., Dreger, D., Larsen, S., Graves, R., Pitarka, A. & Olsen, K.B., 2003. Test of 3D elastodynamic codes, Tech. Rep.2, Pacific Earthquake Engineering Research Center.

Day, S.M., Bielak, J., Dreger, D., Larsen, S., Graves, R., Pitarka, A. & Olsen, K.B., 2005. 3D ground motion simulation in basins, Tech. Rep. 3, Pacific Earthquake Engineering Research Center.

Day, S.M., Bielak, J., Dreger, D., Graves, R., Larsen, S., Olsen, K.B., Pitarka, A. & Ramírez-Guzmán, L., 2006. Numerical simulation of basin effects on long-period ground motion, in *Proceedings of the 8th National Conference on Earthquake Engineering,* Earthquake Engineering Research Institute, San Francisco, California.

Day, S.M., Graves, R.W., Bielak, J., Dreger, D., Larsen, S., Olsen, K.B. adn Pitarka, A. & Ramírez-Guzmán, L., 2008. Model for basin effects on long-period response spectra in southern California, *Earthq. Spectra,* **24**(1), 257–277.

Faccioli, E., Maggio, F., Paolucci, R. & Quarteroni, A., 1997. 2D and 3D elastic wave propagation by a pseudo-spectral domain decomposition method, *J. Seismol.,* **1**(3), 237–251.

Frankel, A. & Stephenson, W., 2000. Three-dimensional simulations of ground motions in the Seattle region for earthquakes in the Seattle fault zone, *Bull. seism. Soc. Am.,* **90**(5), 1251–1267.

Frankel, A. & Vidale, J., 1992. A three-dimensional simulation of seismic waves in the Santa Clara Valley, California, from a Loma Prieta aftershock, *Bull. seism. Soc. Am.,* **82**(5), 2045–2074.

Furumura, T. & Koketsu, K., 2000. Parallel 3-D simulation of ground motion for the 1995 Kobe earthquake: the component decomposition approach, *Pure appl. Geophys.,* **157**(11–12), 2047–2062.

Gottschammer, E. & Olsen, K.B., 2001. Accuracy of the explicit planar free-surface boundary condition implemented in a fourth-order staggered-grid velocity-stress finite-difference scheme, *Bull. seism. Soc. Am.,* **91**(3), 617–623.

Graves, R.W., 1996a. Simulating seismic wave propagation in 3D elastic media using staggered-grid finite differences, *Bull. seism. Soc. Am.,* **86**(4), 1091–1106.

Graves, R.W., 1996b. Simulating realistic earthquake ground motions in regions of deep sedimentary basins, in *Proceedings of the 11th World Conference on Earthquake Engineering,* International Association for Earthquake Engineering, Elsevier Science Ltd., Acapulco, Mexico.

Graves, R.W., 1998. Three-dimensional finite-difference modeling of the San Andreas fault: source parameterization and ground-motion levels, *Bull. seism. Soc. Am.,* **88**(4), 881–897.

Graves, R.W., 2008. The seismic response of the San Bernardino basin region during the 2001 Big Bear lake earthquake, *Bull. seism. Soc. Am.,* **98**(1), 241–252.

Graves, R.W. & Day, S.M., 2003. Stability and accuracy analysis of coarse-grain viscoelastic simulations, *Bull. seism. Soc. Am.,* **93**(1), 283–300.

Graves, R.W. & Pitarka, A., 2004. Broadband time history simulation using a hybrid approach, in *Proceedings of the 13th World Conference on Earthquake Engineering,* International Association for Earthquake Engineering, Vancouver, British Columbia, Canada, Paper 1098.

Graves, R.W., Aagaard, B.T., Hudnut, K., Star, L.M., Stewart, J.P. & Jordan, T.H., 2008. Broadband simulations for M_w 7.8 southern San Andreas earthquakes: ground motion sensitivity to rupture speed, *Geophys. Res. Lett.,* **35,** L22302, doi:10.1029/2008GL035750.

Hauksson, E., 2000. Crustal structure and seismicity distribution adjacent to the Pacific and North America plate boundary in southern California, *J. geophys. Res.,* **105**(B6), 13 875–13 904.

Hauksson, E. & Haase, J.S., 1997. Three-dimensional V_p and v_p/v_s velocity models of the Los Angeles basin and central Transverse Ranges, California, *J. geophys. Res.,* **102**(B3), 5423–5453.

Hisada, Y. & Bielak, J., 2003. A theoretical method for computing near-fault ground motions in layered half-spaces considering static offset due to surface faulting, with a physical interpretation of fling step and rupture directivity, *Bull. seism. Soc. Am.,* **93**(3), 1154–1168.

Hisada, Y., Aki, K. & Teng, T.-L., 1993. 3-D simulations of surface wave propagation in the Kanto sedimentary basin, Japan. Part 2: application of the surface wave BEM, *Bull. seism. Soc. Am.,* **83**(6), 1700–1720.

Jones, L.M. *et al.,* 2008. The ShakeOut scenario, Tech. Rep. USGS-R1150, CGS-P25, U.S. Geological Survey and California Geological Survey.

Käser, M. & Dumbser, M., 2006. An arbitrary high-order discontinuous galerkin method for elastic waves on unstructured meshes—I. The two-dimensional isotropic case with external source terms, *Geophys. J. Int.,* **166**(2), 855–877.

Käser, M. & Gallovic, F., 2008. Effects of complicated 3D rupture geometries on earthquake ground motion and their implications: a numerical study, *Geophys. J. Int.,* **172**(1), 276–292.

Kawase, H. & Aki, K., 1990. Topography effect at the critical *SV*-wave incidence: possible explanation of damage pattern by the Whittier Narrows, California, earthquake of 1 October 1987, *Bull. seism. Soc. Am.,* **80**(1), 1–22.

Kelly, K.R., Ward, R.W., Treitel, S. & Alford, R.M., 1976. Synthetic seismograms: a finite-difference approach, *Geophysics,* **41**(1), 2–27.

Kleindorfer, G.B. & Ganeshan, R., 1993. The philosophy of science and validation in simulation, in *Proc. 1993 Winter Simulation Conf.,* pp. 50–57, eds Evans, G.W., Mollaghasemi, M., Russell, E.C. & Biles, W.E., Los Angeles, CA.

Kohler, M.D., Magistrale, H. & Clayton, R.W., 2003. Mantle heterogeneities and the SCEC reference three-dimensional seismic velocity model version 3, *Bull. seism. Soc. Am.,* **93**(2), 757–774.

Komatitsch, D. & Tromp, J., 1999. Introduction to the spectral element method for three-dimensional seismic wave propagation, *Geophys. J. Int.,* **139**(3), 806–822.

Komatitsch, D. & Vilotte, J.-P., 1998. The spectral element method: an efficient tool to simulate the seismic response of 2D and 3D geological structures, *Bull. seism. Soc. Am.,* **88**(2), 368–392.

Komatitsch, D., Liu, Q., Tromp, J., Suss, P., Stidham, C. & Shaw, J.H., 2004. Simulations of ground motion in the Los Angeles basin based upon the spectral-element method, *Bull. seism. Soc. Am.,* **94**(1), 187–206.

Kristek, J. & Moczo, P., 2003. Seismic-wave propagation in viscoelastic media with material discontinuities: a 3D fourth-order staggered-grid finite-difference modeling, *Bull. seism. Soc. Am.,* **93**(5), 2273–2280.

Kristek, J., Moczo, P. & Archuleta, R., 2002. Efficient methods to simulate planar free surface in the 3D 4th-order staggered-grid finite-difference schemes, *Stud. Geophys. Geod.,* **46**(2), 355–381.

Kristekova, M., Kristek, J., Moczo, P. & Day, S.M., 2006. Misfit criteria for quantitative comparison of seismograms, *Bull. seism. Soc. Am.,* **96**(5), 1836–1850.

Levander, A.R., 1988. Fourth-order finite-difference *P-SV seismograms, Geophysics,* **53**(11), 1425–1436.

Lysmer, J. & Drake, L.A., 1972. A finite element method for seismology, in *Methods in Computational Physics,* **Vol. 11**, chap. 6, eds Alder, B., Fernbach, S. & Bolt, B., Academic Press, New York.

Lysmer, J. & Kuhlemeyer, R.L., 1969. Finite dynamic model for infinite media, *J. Eng. Mech. Div., ASCE,* **95**(EM4), 859–877.

Magistrale, H., McLaughlin, K. & Day, S., 1996. A geology-based 3D velocity model of the Los Angeles basin sediments, *Bull. seism. Soc. Am.,* **86**(4), 1161–1166.

Magistrale, H., Day, S., Clayton, R.W. & Graves, R., 2000. The SCEC southern California reference three-dimensional seismic velocity model version 2, *Bull. seism. Soc. Am.,* **90**(6B), S65–S76.

Marcinkovich, C. & Olsen, K., 2003. On the implementation of perfectly matched layers in a three-dimensional fourth-order velocity-stress finite difference scheme, *J. geophys. Res.,* **108**(B5), 2276, doi:10.1029/2002JB002235.

Meza-Fajardo, K.C. & Papageorgiou, A.S., 2008. A nonconvolutional, split-field, perfectly matched layer for wave propagation in isotropic and anisotropic elastic media: stability analysis, *Bull. seism. Soc. Am.,* **98**(4), 1811–1836.

Moczo, P., Kristek, J., Vavryuk, V., Archuleta, R.J. & Halada, L., 2002. 3D heterogeneous staggered-grid finite-difference modeling of seismic motion with volume harmonic and arithmetic averaging of elastic moduli and densities, *Bull. seism. Soc. Am.,* **92**(8), 3042–3066.

Moczo, P., Kristek, J., Galis, M., Pazk, P. & Balazovjech, M., 2007. The finite-difference and finite-element modeling of seismic wave propagation and earthquake motion, *Acta Phys. Slovaca,* **57**(2), 177–406.

Mossessian, T.K. & Dravinski, M., 1987. Application of a hybrid method for scattering of *P*, *SV*, and Rayleigh waves by near-surface irregularities, *Bull. seism. Soc. Am.,* **77**(5), 1784–1803.

Olsen, K.B., 1994. Simulation of three-dimensional wave propagation in the Salt Lake basin, *PhD thesis*, University of Utah, Salt Lake City, Utah.

Olsen, K.B. & Archuleta, R.J., 1996. Three-dimensional simulation of earthquakes on the Los Angeles fault system, *Bull. seism. Soc. Am.,* **86**(3), 575–596.

Olsen, K.B., Archuleta, R.J. & Matarese, J.R., 1995a. Three-dimensional simulation of a magnitude 7.75 earthquake on the San Andreas fault, *Science,* **270**(5242), 1628–1632.

Olsen, K.B., Pechmann, J.C. & Schuster, G.T., 1995b. Simulation of 3D elastic wave propagation in the Salt Lake basin, *Bull. seism. Soc. Am.,* **85**(6), 1688–1710.

Olsen, K.B. *et al.,* 2006. Strong shaking in Los Angeles expected from southern San Andreas earthquake, *Geophys. Res. Lett.,* **33**(L07305), 1–4.

Olsen, K.B., Day, S.M., Minster, J.B., Cui, Y., Chourasia, A., Okaya, D., Maechling, P. & Jordan, T., 2008. TeraShake2: spontaneous rupture simulations of M_W 7.7 earthquakes on the southern San Andreas fault, *Bull. seism. Soc. Am.,* **98**(3), 1162–1185.

Olsen, K.B. *et al.,* 2009. ShakeOut-D: ground motion estimates using an ensemble of large earthquakes on the southern San Andreas fault with spontaneous rupture propagation, *Geophys. Res. Lett.,* **36,** L04303, doi:10.1029/2008GL036832.

Oreskes, N., Shrader-Frechette, K. & Belitz, K., 1994. Verification, validation, and confirmation of numerical models in the earth sciences, *Science,* **263**(5147), 641–646.

Pitarka, A., Irikura, K., Iwata, T. & Sekiguchi, H., 1998. Three-dimensional simulation of the near-fault ground motion for the 1995 Hyogo-Ken Nanbu (Kobe), Japan, earthquake, *Bull. seism. Soc. Am.,* **88**(2), 428–440.

Rodgers, A., Petersson, N.A., Nilsson, S., Sjogreen, B. & McCandless, K., 2008. Broadband waveform modeling of moderate earthquakes in the San Francisco bay area and preliminary assessment of the USGS 3D seismic velocity model, *Bull. seism. Soc. Am.,* **98**(2), 969–988.

Rust, D., 2005. Palaeoseismology in steep terrain: the big bend of the San Andreas fault, Transverse Ranges, California, *Tectonophysics,* **408**(1–4), 193–212.

Sánchez-Sesma, F.J. & Luzón, F., 1995. Seismic response of three-dimensional alluvial valleys for incident *P*, *S*, and Rayleigh waves, *Bull. seism. Soc. Am.,* **85**(1), 269–284.

Sargent, R.G., 2005. Verification and validation of simulation models, in *Proc. 2005 Winter Simulation Conf.,* pp. 130–143, eds Kuhl, M.E., Steiger, N.M., Armstrong, F.B., Joines, J.A., Orlando, FL, doi:10.1109/WSC.2005.1574246.

Schlesinger, S. *et al.,* 1979. Terminology for model credibility, *Simulation,* **32**(3), 103–104.

Schlosser, S.W., Ryan, M.P., Taborda, R., López, J., O'Hallaron, D. & Bielak, J., 2008. Materialized community ground models for large-scale earthquake simulation, in *Proceedings of the 2008 ACM/IEEE International Conference for High Performance Computing, Networking, Storage and Analysis,* p. 11, IEEE Computer Society, Austin, Texas.

Seriani, G., 1998. 3-D large-scale wave propagation modeling by spectral element method on Cray T3E multiprocessor, *Comput. Methods Appl. Mech. Eng.,* **64**(1–2), 235–247.

Seriani, G. & Priolo, E., 1994. Spectral element method for acoustic wave simulation in heterogeneous media, *Finite Elements Anal. Des.,* **16**(3–4), 337–348.

Sieh, K., 1978. Slip along the San Andreas fault associated with the great 1857 earthquake, *Bull. seism. Soc. Am.,* **68**(5), 1421–1448.

Sieh, K., 1986. Slip rate across the San Andreas fault and prehistoric earthquakes at Indio, California, *EOS, Trans. Am. geophys. Un.,* **67,** 1200.

Süss, M.P. & Shaw, J.H., 2003. *P* wave seismic velocity structure derived from sonic logs and industry reflection data in the Los Angeles basin, California, *J. geophys. Res.,* **108**(B3), 2170, doi:10.1029/2001JB001628.

Taborda, R., López, J., O'Hallaron, D., Tu, T. & Bielak, J., 2007. A review of the current approach to CVM-Etrees, in *Proceedings and Abstracts of the 2007 SCEC Annual Meeting,* http://www.ce.cmu.edu/∼rtaborda.

Tu, T., López, J. & O'Hallaron, D., 2003. The etree library: a system for manipulating large octrees on disk, Tech. Rep. CMU-CS-03-174, School of Computer Science, Carnegie Mellon University, Pittsburgh, Pennsylvania.

Tu, T., Yu, H., Ramírez-Guzmán, L., Bielak, J., Ghattas, O., Ma, K.-L., & O'Hallaron, D.R., 2006. From mesh generation to scientific visualization: an end-to-end approach to parallel supercomputing, in *Proceedings of the 2006 ACM/IEEE International Conference for High Performance Computing, Networking, Storage and Analysis,* p. 15, IEEE Computer Society, Tampa, Florida.

Wills, C.J., Weldon, R.J. II, & Bryant, W.A., 2008. California fault parameters for the National Seismic Hazard Maps and Working

Group on California Earthquake Probabilities 2007, in The Uniform California Earthquake Rupture Forecast, Version 2 (UCERF 2), no. USGS-OFR-2007-1437, CGS SR-203, chap. Appendix A, p.51, ed. Working Group on California Earthquake Probabilities, U.S. Geological Survey and California Geological Survey.

Working Group on California Earthquake Probabilities, 2008. The uniform California earthquake rupture forecast, Version 2 (UCERF 2), Tech. Rep. USGS OFR-2007-1437, CGS SR-203, SCEC C-1138, U.S. Geological Survey in cooperation with the California Geological Survey and the Southern California Earthquake Center.